The Astronomical Journal, 162:283 (22pp), 2021 December https://doi.org/10.3847/1538-3881/ac1bbe

A Pair of Warm Giant Planets near the 2:1 Mean Motion Resonance around the K-dwarf Star TOI-2202*

Trifon Trifonov[1], Rafael Brahm[2,3], Nestor Espinoza[4], Thomas Henning[1], Andrés Jordán[2,3], David Nesvorny[5], Rebekah I. Dawson[6], Jack J. Lissauer[7], Man Hoi Lee[8,9], Diana Kossakowski[1], Felipe I. Rojas[3,10], Melissa J. Hobson[3,10], Paula Sarkis[1], Martin Schlecker[1], Bertram Bitsch[1], Gaspar Á. Bakos[11,12,28], Mauro Barbieri[13], W. Bhatti[11], R. Paul Butler[14], Jeffrey D. Crane[15], Sangeetha Nandakumar[13], Matías R. Díaz[16,17], Stephen Shectman[15], Johanna Teske[14], Pascal Torres[3,10], Vincent Suc[18], Jose I. Vines[16], Sharon X. Wang[15,19], George R. Ricker[20], Avi Shporer[20], Andrew Vanderburg[21], Diana Dragomir[22], Roland Vanderspek[20], Christopher J. Burke[20], Tansu Daylan[20,29], Bernie Shiao[23], Jon M. Jenkins[24], Bill Wohler[24,25], Sara Seager[20,26,27], and Joshua N. Winn[11]

[1] Max-Planck-Institut für Astronomie, Königstuhl 17, D-69117 Heidelberg, Germany; trifonov@mpia.de
[2] Facultad de Ingeniera y Ciencias, Universidad Adolfo Ibáñez, Av. Diagonal las Torres 2640, Peñalolén, Santiago, Chile
[3] Millennium Institute for Astrophysics, Chile
[4] Space Telescope Science Institute, 3700 San Martin Drive, Baltimore, MD 21218, USA
[5] Department of Space Studies, Southwest Research Institute, 1050 Walnut Street, Suite 300, Boulder, CO 80302, USA
[6] Department of Astronomy & Astrophysics, Center for Exoplanets and Habitable Worlds, The Pennsylvania State University, University Park, PA 16802, USA
[7] Space Science & Astrobiology Division MS 245-3 NASA Ames Research Center, Moffett Field, CA 94035, USA
[8] Department of Earth Sciences, The University of Hong Kong, Pokfulam Road, Hong Kong
[9] Department of Physics, The University of Hong Kong, Pokfulman Road, Hong Kong
[10] Instituto de Astrofísica, Facultad de Física, Pontificia Universidad Católica de Chile, Chile
[11] Department of Astrophysical Sciences, Princeton University, NJ 08544, USA
[12] Institute for Advanced Study, 1 Einstein Drive, Princeton, NJ 08540, USA
[13] INCT, Universidad de Atacama, calle Copayapu 485, Copiapó, Atacama, Chile
[14] Carnegie Institution for Science, Earth & Planets Laboratory, 5241 Broad Branch Road NW, Washington, DC 20015, USA
[15] The Observatories of the Carnegie Institution for Science, 813 Santa Barbara Street, Pasadena, CA 91101, USA
[16] Departamento de Astronomía, Universidad de Chile, Camino El Observatorio 1515, Las Condes, Santiago, Chile
[17] Las Campanas Observatory, Carnegie Institution for Science, Colina El Pino, Casilla 601, La Serena, Chile
[18] Instituto de Astrofísica, Pontificia Universidad Católica de Chile, Av. Vicuña Mackenna 4860, 7820436 Macul, Santiago, Chile
[19] Department of Astronomy, Tsinghua University, Beijing 100084, People's Republic of China
[20] Department of Physics and Kavli Institute for Astrophysics and Space Research, Massachusetts Institute of Technology, Cambridge, MA 02139, USA
[21] Department of Astronomy, University of Wisconsin-Madison, Madison, WI 53706, USA
[22] Department of Physics and Astronomy, University of New Mexico, 1919 Lomas Boulevard NE, Albuquerque, NM 87131, USA
[23] Space Telescope Science Institute, 3700 San Martin Drive, Baltimore, MD, 21218, USA
[24] NASA Ames Research Center, Moffett Field, CA 94035, USA
[25] SETI Institute, Mountain View, CA 94043, USA
[26] Department of Earth, Atmospheric and Planetary Sciences, Massachusetts Institute of Technology, Cambridge, MA 02139, USA
[27] Department of Aeronautics and Astronautics, MIT, 77 Massachusetts Avenue, Cambridge, MA 02139, USA
Received 2021 April 25; revised 2021 July 29; accepted 2021 August 3; published 2021 December 2

Abstract

TOI-2202 b is a transiting warm Jovian-mass planet with an orbital period of $P = 11.91$ days identified from the Full Frame Images data of five different sectors of the TESS mission. Ten TESS transits of TOI-2202 b combined with three follow-up light curves obtained with the CHAT robotic telescope show strong transit timing variations (TTVs) with an amplitude of about 1.2 hr. Radial velocity follow-up with FEROS, HARPS, and PFS confirms the planetary nature of the transiting candidate ($a_b = 0.096 \pm 0.001$ au, $m_b = 0.98 \pm 0.06$ M_{Jup}), and a dynamical analysis of RVs, transit data, and TTVs points to an outer Saturn-mass companion ($a_c = 0.155 \pm 0.002$ au, $m_c = 0.37 \pm 0.10$ M_{Jup}) near the 2:1 mean motion resonance. Our stellar modeling indicates that TOI-2202 is an early K-type star with a mass of 0.82 $M_\odot$, a radius of 0.79 $R_\odot$, and solar-like metallicity. The TOI-2202 system is very interesting because of the two warm Jovian-mass planets near the 2:1 mean motion resonance, which is a rare configuration, and their formation and dynamical evolution are still not well understood.

Unified Astronomy Thesaurus concepts: Exoplanet astronomy (486)

1. Introduction

The past twenty-five years of exoplanet searches have resulted in over 4300 confirmed planets, including over 700[30] systems with multiple planets. The physical characteristics of the discovered exoplanet systems show a great contrast with those of the solar system. Of course, the observed diversity of exoplanet populations is still a subject of observational biases

* Based on observations collected at the European Organization for Astronomical Research in the Southern Hemisphere under ESO programs 0104.C–0413 and 1102.C–0923, and MPG programs 0102.A–9006, 0103.A–9008, and 0104.A–9007. This paper includes data gathered with the 6.5 meter Magellan Telescopes located at Las Campanas Observatory, Chile.

[28] Packard Fellow.

[29] Kavli Fellow.

[30] Up-to-date list available on https:exoplanet.eu.

(see, e.g., Fischer et al. 2014). For instance, the two most successful exoplanet detection techniques—the transit method and the radial velocity (RV) method—are capable of detecting short-period planets as small as Earth. The longest-running RV surveys have a sufficient temporal baseline to detect long-period planets (Bonfils et al. 2013; Reffert et al. 2015; Butler et al. 2017; Udry et al. 2019; Wittenmyer et al. 2020), but the achievable precision is only sufficient to detect Jovian planets, or at best, Saturn-mass planets. But despite the known biases, we can still use the current observational exoplanet data to fine-tune the applicable planet formation theories in an attempt to understand the planet formation mechanisms in general.

The discovery of very close-orbiting planets, planets on eccentric orbits, and pairs of planets in mean motion resonances (MMRs) have led to major developments in the theory of the formation and dynamical evolution of planets, and in particular, in our understanding of the importance of interactions between planets and the protoplanetary disk (Ida & Lin 2010; Kley & Nelson 2012; Baruteau et al. 2014; Coleman & Nelson 2014; Levison et al. 2015; Bitsch et al. 2020; Schlecker et al. 2020b; Matsumura et al. 2021). One of the long-standing challenges in the field of exoplanets is to explain the origin of the population of giant planets with orbits interior to the so-called snow line. These objects are not easily understood within standard formation models that require rapid accretion of gas by a solid embryo before the stellar radiation dissipates the gas from the protoplanetary disk. This rapid, solid accretion is favored beyond the snow line. Giant planets are expected then to migrate from a couple of astronomical units to the inner regions of the system to produce the population of hot ($P < 10$ days) and warm (10 days $< P <$ 300 days) Jovian-mass planets. Typical migration mechanisms can be divided in two groups, namely: disk migration (e.g., Lin & Papaloizou 1986) and high eccentricity tidal migration (e.g., Rasio & Ford 1996; Fabrycky & Tremaine 2007; Bitsch et al. 2020). Both types of mechanisms predict significantly different orbital configurations for the migrating planet, and the characterization of these properties, particularly on warm Jovians (Huang et al. 2016; Petrovich & Tremaine 2016; Santerne et al. 2016; Dong et al. 2021), can be used to constrain migration theories.

Gas accretion is thought to be faster beyond the ice line because the cores would be large enough. Nonetheless, given the high frequency of sufficiently large "cores" (i.e., super-Earths and mini-Neptunes) discovered close to their star, the in-situ formation of giant planets is also a possible scenario (e.g., Batygin et al. 2016). In addition, planets can also be scattered toward warmer orbits via violent gravitational interactions and instabilities (e.g., Ford et al. 2005).

In this context, it is fundamentally important to measure the dynamical mass and orbital eccentricity of the warm Jovian planets. For many systems, this can only be achieved by combining precise transit and RV observational exoplanet data. NASA's Transiting Exoplanet Survey Satellite (TESS; Ricker et al. 2015) aims to detect planets through the transit method around relatively bright stars that are suitable for precise Doppler follow-up to determine the planetary mass, radius, and bulk density, among other important physical parameters. TESS has already led to more than 130 new discovered planets, most of which were confirmed by Doppler spectroscopy (e.g., Dumusque et al. 2019; Kossakowski et al. 2019; Luque et al. 2019; Trifonov et al. 2019a; Wang et al. 2019; Espinoza et al. 2020; Schlecker et al. 2020a; Teske et al. 2020, among many).

In this paper, we report the discovery of a warm Jovian-mass planet pair around the K-dwarf star TOI-2202 (TIC 358107516[31]). The inner planet TOI-2202 b shows unambiguous transit events with a period of 11.9 days, recorded by TESS and ground-based photometry. The strong transit timing variations (TTVs) of the transiting planet and the precise RV measurements we obtained for this target revealed the existence of an additional outer Saturn-mass planet TOI-2202 c with an orbital period of 24.7 days, thus forming a planet pair close to the 2:1 MMR. This discovery was made in the context of the Warm gIaNts with tEss (WINE) collaboration, which focuses on the systematic characterization of TESS transiting warm giant planets (e.g., Brahm et al. 2019, 2020; Jordán et al. 2020; Schlecker et al. 2020a).

In Section 2 we present our stellar parameter estimates of TOI-2202. In Section 3 we present the transit photometry and Doppler observational data used to characterize the TOI-2202 multiple-planet system. In Section 4 we describe our orbital analysis using a self-consistent dynamical modeling scheme, whereas in Section 5 we comment on the dynamical and long-term stability properties of the TOI-2202 system. Section 6 is for our summary and conclusions.

2. Data

2.1. Transit Photometry

2.1.1. TESS

TOI-2202 was observed in five out of the 13 Sectors of the first year of the TESS primary mission. Observations were performed with the 30 minute cadence mode in Sectors 1, 2, 6, 9, and 13 between 2018 and 2019 July. TOI-2202 b was identified in the light curves extracted from the TESS Full Frame Images (FFIs). This was done using a pipeline called `tesseract`[32] (F. Rojas et al. 2021, in preparation). Pipeline `tesseract` receives the TIC ID as input and performs simple aperture photometry on the FFIs via the `TESSCut` (Brasseur et al. 2019) and `lightkurve` (Lightkurve Collaboration et al. 2018) packages. In the context of the WINE collaboration, we generated light curves for all Sectors of the first year of the TESS primary mission for stars in the TICv8 catalog brighter than $T = 13$ mag. Transiting candidates are identified by running the `transitleastsquares` package (TLS; Hippke & Heller 2019) on each light curve, and also by searching for individual negative deviations from the median flux. This latter processing allowed us to identify long-period planets (e.g., Schlecker et al. 2020a) and single transiters (Gill et al. 2020). TOI-2202 was identified as a candidate in individual TESS light curves using both detection methods, finding a periodicity of the transits of ∼12 days. Figure 1 shows the target pixel file (TPF) image of TOI-2202 constructed from the TESS image frames and Gaia DR2 data. We investigated if the transit signal was coming from neighboring stars by generating light curves for each of the pixels in a region 20 pixels wide around the target star, and also by analyzing the time series associated with the background flux. We found that the signal indeed originated close ($<2'$) to

[31] The target became a TESS Object of Interest (TOI, Guerrero et al. 2021) while this work was in an advanced stage. Our discovery is based on the TESS Full Frame Image data, adopting the target designation TIC 358107516 (see Section 2.1.1). Consequently, we adopted the TOI-2202 designation for consistency with the TESS survey.

[32] https://github.com/astrofelipe/tesseract

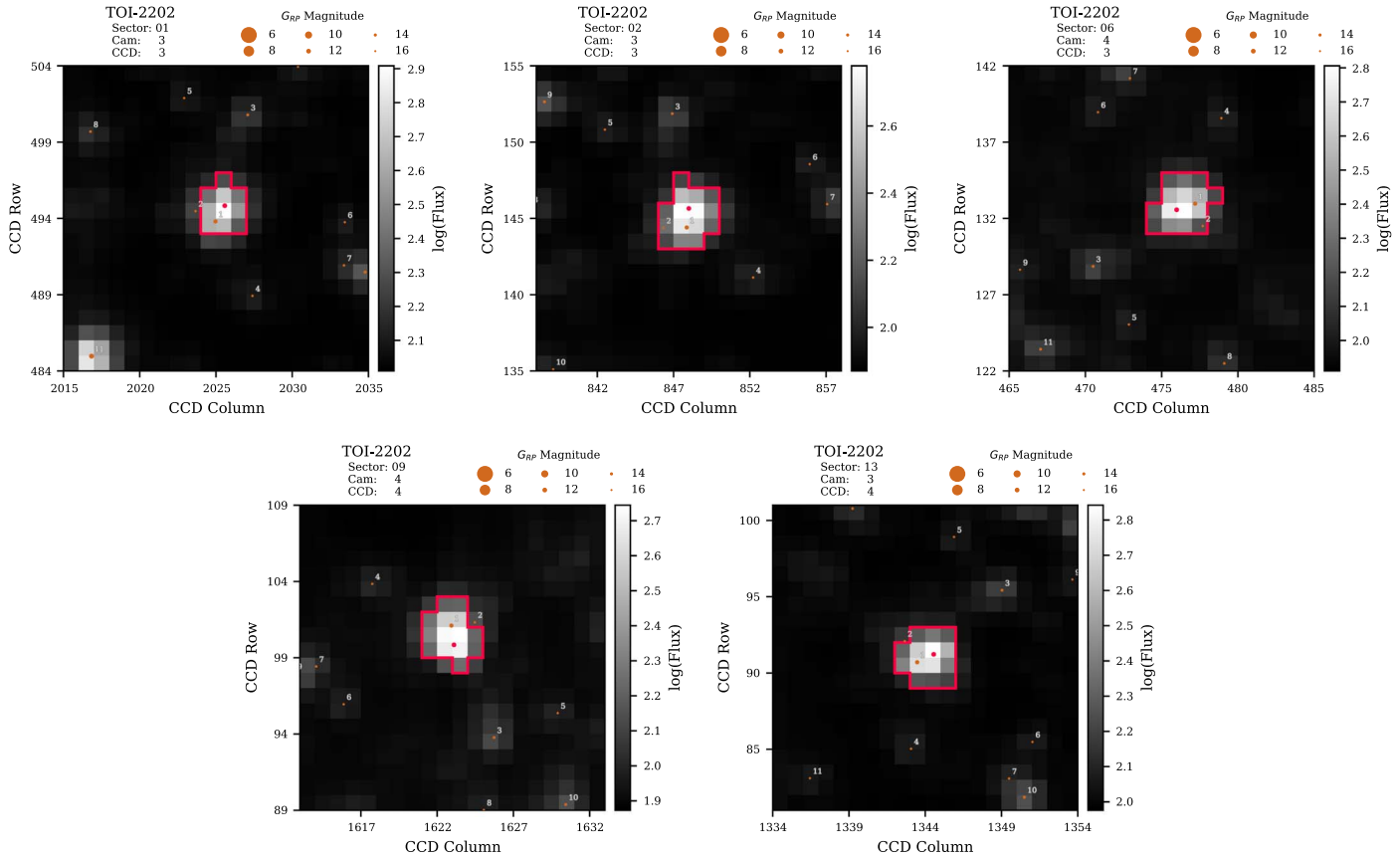

Figure 1. Target pixel file (TPF) image of TOI-2202 in TESS Sector 2. The red dots show the position of TOI-2202 (brighter) and the neighbor star TIC 358107518 (fainter). The red borders in the pixel space are the one used to construct the TESS Simple Aperture Photometry (SAP). Gaia targets are marked with orange circles, with sizes coded by their G magnitude.

the target star. Nonetheless, as is shown in Figure 1, TOI-2202 has a slightly fainter ($T = 12.7$) neighboring star located at $\sim 24''$ from it (TIC358107518) that was not possible to fully reject as the source of the observed transits. Our ground-based photometric and Doppler follow-up confirmed that the source of the transit signal was indeed TOI-2202 (see Sections 2.1.2 and 2.2).

Since `tesseract` does not correct for contamination in the TESS apertures from nearby stars, we also apply a dilution correction for the contamination of TIC 358107518. To estimate the dilution, we use the $R-P$ Gaia DR3 fluxes of TOI-2202 and TIC 358107518, and Equation (6) in Espinoza et al. (2019). For TOI-2202 the mean $R-P$ flux is 113,856 electron s^{-1}, while the mean $R-P$ flux of TIC 358107518 is 66,547 electron s^{-1}, and we obtain a dilution factor of 0.63, which was applied to the light curves.

The top panel of Figure 2 shows the dilution-corrected, median-normalized, TESS FFI light curves of TOI-2202. All of the TESS 30 minute cadence FFI data taken in Sectors 1, 2, 6, 9, and 13 suffered from notable systematics, which could be attributed to stellar activity, instrumental effects, or a combination of both. The transit events with a depth of approximately 1%, which was consistent with being produced by a Jupiter-sized planet with a period of about 11.9 days, can be also easily identified on the combined TESS light curve. The bottom panel of Figure 2 shows a GLS periodogram of the TESS light curve with prominent peaks in the range between 20 and 30 days, which come from the light-curve systematics, and which are generally in line with the most likely rotational period range of TOI-2202 (see Section 3).

2.1.2. CHAT

After we detected the transit events in the TESS FFIs of TOI-2202, we scheduled photometric monitoring from the ground with the 0.7 m Chilean–Hungarian Automated Telescope (CHAT) installed at Las Campanas Observatory, in Chile. We obtained four light curves on four different nights between 2019 February and November. All observations were performed in the Sloan i' band with exposure times of 150 s. The data were reduced and processed into differential photometry light curves with a dedicated package (e.g., Kossakowski et al. 2019; Jordán et al. 2019).

The transit signal of the TOI-2202 b planet candidate was detected on three of the four light curves. (two partial transits in ingress, and a single full transit), which allowed us to confirm that the transits do not occur on the slightly fainter close companion, to refine the transit parameters, and to further characterize the transit timing variations of the system. The CHAT follow-up data are available in electronic form in ExoFOP at https://exofop.ipac.caltech.edu/tess/target.php?id=358107516, and the light curves are displayed in Figure 7.

2.2. RV Data

2.2.1. FEROS

We conducted a spectroscopic follow-up campaign for TOI-2202 between 2019 February and November with the FEROS

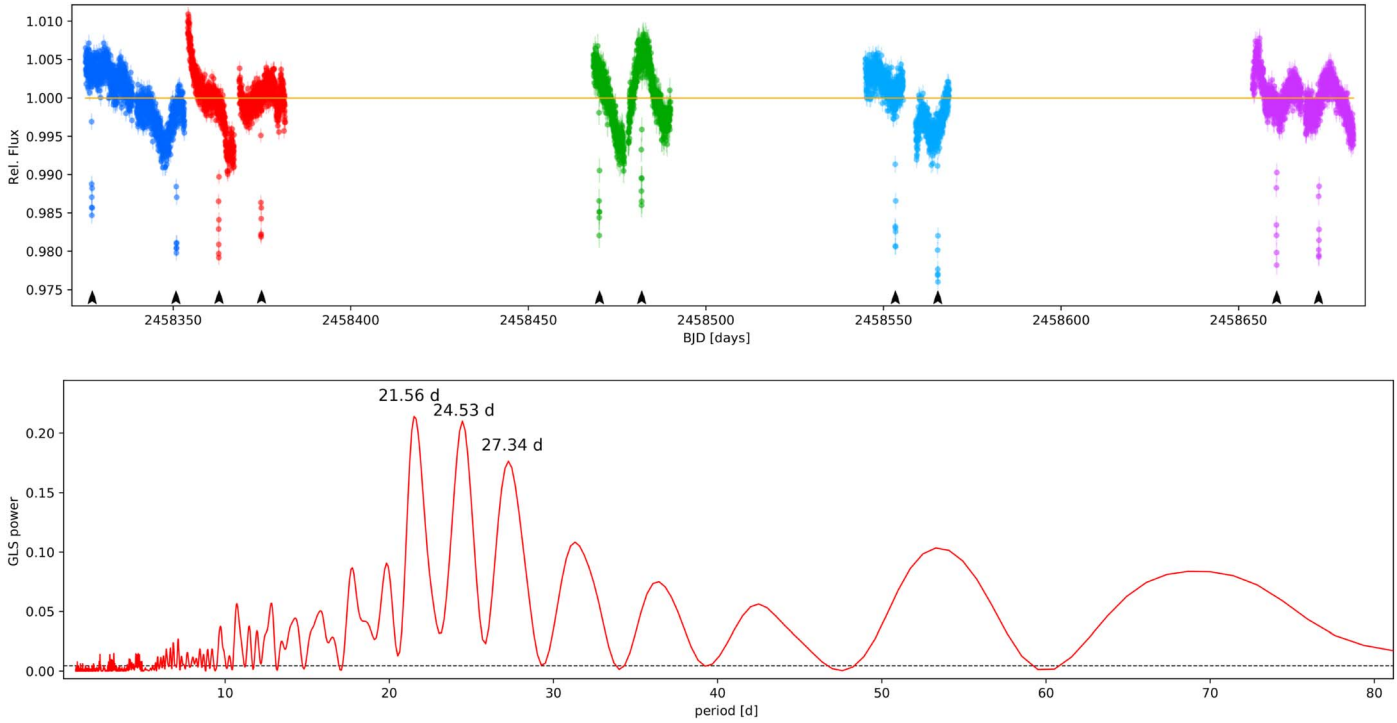

Figure 2. The top panel shows the raw TESS photometry data of TOI-2202 reduced with `tesseract` and normalized to its median. TESS data from Sectors 1 (blue), 2 (red), 6 (green), 9 (cyan), and 13 (magenta) clearly show transit events with a period of ∼11.91 days, but also exhibit periodic systematics, which could be attributed to stellar activity, instrumental effects, or a combination of both. The bottom panel shows the GLS periodogram of the raw TESS data, yielding prominent peaks in the range between 20 and 30 days. The dashed line is the 0.1% FAP.

spectrograph (Kaufer et al. 1999) installed at the ESO-MPG 2.2 m telescope at La Silla Observatory. Our immediate objective for the FEROS observations was to determine if the transit-like signals present in the stellar light curve were indeed produced by a transiting Jovian companion. In total we obtained 26 FEROS spectra with exposure times of 1200 and 1500 s, delivering signal-to-noise (S/N) ratios per resolution element ranging from 20 to 60. Observations were performed with the simultaneous calibration technique, in conjunction with a ThAr calibration lamp. FEROS data were reduced, extracted, and analyzed with the `ceres` pipeline (Brahm et al. 2017a) delivering RV and bisector span measurements with a typical uncertainty of $\sim$15 m s^{-1}. The obtained RVs are tabulated in Table A1 and displayed in Figures 5 and 6 as a function of time and orbital phase. These FEROS RVs allowed the identification of a Keplerian signal with a period consistent with that of the transiting events of TESS and CHAT, and an amplitude compatible with a Jovian-mass object.

2.2.2. HARPS

The High Accuracy Radial velocity Planet Searcher (HARPS, Mayor et al. 2003) is an ultra-stable high-resolution ($R = 115{,}000$) échelle spectrograph mounted at the 3.6 m telescope of the European Southern Observatory (ESO) in La Silla, Chile. HARPS is capable of delivering stellar RV measurements with a precision down to $\sim$1 m s^{-1}.

We obtained 21 spectra with HARPS between 2019 June and 2020 February. We adopted an exposure time of 1800 s, which translated to spectra with an S/N of ∼25. We retrieved precise RV measurements derived by the ESO-DRS pipeline, which uses a spectrum cross-correlation function (CCF) method with a weighted binary mask (Pepe et al. 2002). The DRS pipeline also provides the CCF's FWHM and the Bisector Inverse Slope span (BIS-span) measurements, which are valuable stellar activity indicators (Queloz et al. 2001). Additionally, we derived precise RVs and stellar activity indicators from the HARPS spectra of TOI-2202 with the SpEctrum Radial Velocity AnaLyser (SERVAL, Zechmeister et al. 2018) pipeline. SERVAL also measures stellar activity indicators such as Hα, Na I D, Na II D, and the differential line width (dLW), quantifying variations in the spectral line widths, and the chromatic RV index (CRX) of the spectra (for a detail description of the SERVAL activity time series measurements, see Zechmeister et al. 2018). We found that, in the case of TOI-2202, the original RVs derived with the ESO-DRS pipeline are somewhat less precise, but overall, more accurate. For instance, the median RV uncertainty of ESO-DRS is $\hat{\sigma_{\rm DRS}} = 7.09$ m s^{-1} and for SERVAL the median RV uncertainty is only $\hat{\sigma_{\rm SERVAL}} = 3.26$ m s^{-1}, but the latter data set contains three very strong outliers at epochs BJDs = 2458773.7777, 2458774.7145, and 2458838.6934. While the rest of the SERVAL and the DRS RVs are generally consistent, we decided to use the larger, more consistent, DRS RV data set for the orbital analysis in our study. The precise RVs and activity index data from SERVAL and DRS are tabulated in Table A2, and will be also available in electronic form in the `HARPS-RVBank ver.02`[33] (Trifonov et al. 2020). A visual inspection of the HARPS-DRS is shown in Figures 5 and 6 as a function of time and orbital phase.

2.2.3. PFS

TOI-2202 was also monitored with the Planet Finder Spectrograph (Crane et al. 2006, 2008, 2010) installed at the

[33] https://github.com/3fon3fonov/HARPS_RVBank, https://www2.mpia-hd.mpg.de/homes/trifonov/HARPS_RVBank.html

Table 1
Stellar Parameters of TOI-2202 and Their 1σ Uncertainties

Parameter	TOI-2202	Reference
Spectral type	K8V	ESA (1997)
Distance (pc)	$235.93^{+1.05}_{-1.04}$	Gaia Collaboration et al. (2016, 2018), Bailer-Jones et al. (2018)
Mass ($M_\odot$)	$0.823^{+0.027}_{-0.023}$ (0.041)	This paper
Radius ($R_\odot$)	$0.794^{+0.007}_{-0.007}$ (0.032)	This paper
Luminosity ($L_\odot$)	$0.397^{+0.014}_{-0.013}$ (0.014)	This paper
Age (Gyr)	$7.48^{+3.32}_{-3.33}$	This paper
A_V (mag)	$0.242^{+0.0056}_{-0.054}$	This paper
$T_{\rm eff}$ (K)	5144 ± 50 (103)	This paper
$\log g$ (cm s^{-2})	4.55 ± 0.20	This paper
[Fe/H]	0.04 ± 0.05	This paper
$v \cdot \sin(i)$ (km s^{-1})	1.7 ± 0.5	This paper

Note. The values in parentheses are the floor uncertainties predicted by Tayar et al. (2020) and adopted in our work. References: (1) ESA (1997), (2) Gaia Collaboration et al. (2016, 2018), (3) Bailer-Jones et al. (2018).

6.5 m Magellan Clay telescope at Las Campanas Observatory. TOI-2202 was observed with the iodine cell in four different epochs between 2019 July and December, adopting an exposure time of 1200 s, and using 3×3 CCD binning mode to minimize read noise. TOI-2202 was also observed without the iodine cell in order to generate the template for computing the RVs, which were derived following the methodology of Butler et al. (1996). The PFS RVs are presented in Table A3 and displayed in Figures 5 and 6.

3. Stellar Parameters of TOI-2202

The atmospheric parameters of TOI-2202 were computed from the co-added HARPS spectra using the `zaspe` package (Brahm et al. 2017b), which delivers $T_{\rm eff}$, $\log g$, [Fe/H], and $v \sin i$ through comparison against a grid of synthetic spectra generated from the ATLAS9 model atmospheres (Castelli & Kurucz 2004).

The physical parameters of TOI-2202 were obtained by using the PARSEC evolutionary models, following the prescription described in Brahm et al. (2019). These models allow us to compare the absolute magnitudes for a given set of stellar parameters to those of the target star by using the distance to the star as obtained from the Gaia DR2 catalog (Gaia Collaboration et al. 2018). For this comparison we used the Gaia G, G_{BP}, and G_{RP}, and the 2MASS J, H, and K_s bands. We fixed the metallicity to the value found with `zaspe` and explored the parameter space for the stellar age and $M_\star$ by using the `emcee` package (Foreman-Mackey et al. 2013). The results of this analysis allowed us to determine a more precise value for the $\log g$ than that of the spectroscopic analysis. We therefore applied an iterative process involving these two procedures in which the output $\log g$ of the spectra energy distribution analysis was given as input for a new `zaspe` run, until convergence was reached.

Our `zaspe` analysis shows that TOI-2202 is probably a late K-type dwarf star with a mass of $0.823^{+0.027}_{-0.023}$ $M_\odot$, a radius of $0.794^{+0.007}_{-0.007}$ $R_\odot$, and solar-like metallicity. The full set of atmospheric and physical parameters are listed in Table 1. However, we note that our relatively small uncertainties in the stellar parameters are internal and do not include possible systematic differences with respect to other stellar models. Therefore, we inflate the stellar uncertainties to more realistic values following the prescription of Tayar et al. (2020). These authors found that for a main-sequence star like TOI-2202, the publicly available model grids suggest a systematic uncertainty floor of order ∼5% in mass, ∼4% in radius, and ∼2% in temperature and luminosity (see Tayar et al. 2020, for more details). The inflated uncertainty estimates are also listed in Table 1 and are the adopted stellar parameter uncertainties through this work.

With an estimated radius of 0.794 ± 0.032 $R_\odot$ and $v \cdot \sin(i)$ 1.7 ± 0.5 km s^{-1}, the most likely stellar rotation period is 26.8 ± 9.0 days, which agrees well with the observed systematic TESS light-curve periodicity, which is likely induced by stellar activity (see Figure 2).

4. Analysis and Results

4.1. Tools

For data and orbital analysis, we employed the `Exo-Striker` exoplanet toolbox[34] (Trifonov 2019). The `Exo-Striker` provides easy access to a large variety of public tools for exoplanet data analysis, such as a generalized Lomb–Scargle periodogram (GLS; Zechmeister & Kürster 2009), a maximum likelihood periodogram (MLP; Baluev 2008, 2009; Zechmeister et al. 2019), transit photometry de-trending via `wotan` (Hippke et al. 2019), and a transit period search via the `transitleastsquares` package (TLS; Hippke & Heller 2019), which we used in this work for the RV and transit photometry signal analysis. The `Exo-Striker` is able to model data with a standard Keplerian model or with a more complex dynamical model in the case of gravitationally interacting multiple-planet systems detected in RVs or transit photometry data. The `Exo-Striker` works in the Jacobi coordinate system, which is a natural frame for the orbital parameterization of multiple-planet systems (Lee & Peale 2003). The modeling can be performed by "best-fit" optimization schemes (i.e., Levenberg–Maquardt, Nelder–Mead, Newton, etc.), sampling schemes such as an affine-invariant ensemble Markov Chain Monte Carlo (MCMC) sampler (Goodman & Weare 2010) via the `emcee` package (Foreman-Mackey et al. 2013), or the nested sampling technique (Skilling 2004) via the `dynesty` sampler (Speagle 2020).

The RV modeling schemes are intrinsic[35] to the `Exo-Striker`, while currently, for transit light-curve models, the `Exo-Striker` employs the BAsic Transit Model cAlculatioN package (`batman`; Kreidberg 2015). In addition, dynamical modeling of TTV data is done with a Python wrapper of the TTV-fast package (Deck et al. 2014). When needed, RV and transit data can be additionally modeled with Gaussian process (GP) regression models using the `celerite` package (Foreman-Mackey et al. 2017a), which is also included in the `Exo-Striker`.

[34] https://github.com/3fon3fonov/exostriker

[35] Some of the available RV routines were originally developed by Tan et al. (2013) for the analysis of the 2:1 MMR system HD 82943, and were further developed for the analysis of the η Ceti, HD 59686, and HD 202696 systems (Trifonov et al. 2014, 2018, 2019b).

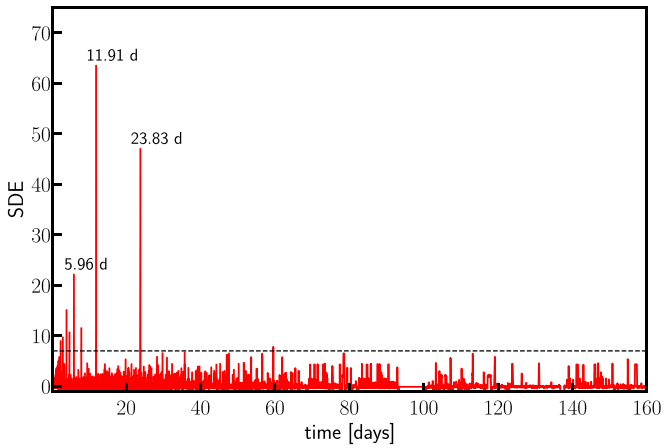

Figure 3. TLS power spectra of the de-trended FFI TESS and CHAT light-curve data of TOI-2202. The planetary transit signal at $P_b = 11.91$ days is accompanied by harmonics at 5.96 days and 23.83 days, etc. The horizontal dashed line indicates the signal detection efficiency (SDE) power level of 7.0, which corresponds to the TLS false positive rate of 1%.

4.2. Transit Light-curve Analysis

We inspected the TESS FFI light curves of TOI-2202 derived with `tesseract`. For our preliminary transit light-curve analysis, we further de-trended each of the `tesseract` sector light curves with a robust (iterative) Matérn GP kernel, with the aim to capture the systematic variation of the light curves (see Hippke et al. 2019). For CHAT data, we applied additional transit photometry de-trending as a function of the airmass at the epoch of observations. Our de-trending scheme resulted in nearly flat, normalized, TESS and CHAT light curves, which we inspected for transits using the TLS algorithm. Figure 3 shows the constructed TLS power spectra of the available transit data of TOI-2202. A significant peak occurs at a period of $P_b = 11.91$ days, followed by peaks at 5.96 days and 23.83 days, etc., which are simply low-order harmonics of the actual transit signal.

However, a single-planet transit model with a period and phase adopted from the TLS failed to produce a good fit to the available TESS and CHAT data. Performing a transit light-curve model optimization by adjusting the orbital period P, eccentricity e and argument of periastron ω (or $e \sin\omega$, $e \cos\omega$), inclination i, time of inferior transit conjunction t_0, the semimajor axis relative to the stellar radius $a/R_\star$, and planetary radius relative to the stellar radius $R/R_\star$ did not help either. We found that the light-curve transit signals exhibit strong deviations in the expected individual time-of-transits assuming a constant period, suggesting strong transit timing variations (TTVs). To extract the TTVs, we performed a separate one-planet fit to the TESS and CHAT light curves, assuming a circular orbit (i.e., $e \sin\omega$, $e \cos\omega_b = 0$), but with variable mid-transit times as fitting parameters. The rest of the transit parameters in this modeling scheme across each individual TESS and CHAT light curve were shared, with exception of the limb-darkening (LD) coefficients of TESS and CHAT, for which we adopted separate quadratic LD models, and nuisance parameters such as the transit light-curve relative photometric offset and additional data jitter.[36] To perform an adequate parameter search, we ran a nested sampling scheme with 1000 "live-points," focused on the posterior convergence instead of Bayesian evidence (see, Speagle 2020, for details). We adopted the 68.3% confidence levels of the nested sampling posterior probability parameter distribution as 1σ parameter uncertainties.

[36] By "jitter," we mean the unknown variance parameter, which is added in quadrature to the transit photometry and RV error budget. See Baluev (2009).

Table 2
Individual Mid-transit Time Estimates of TOI-2202 b

N Transit	t_0 (BJD)	σ t_0 (BJD)	Instrument
1	2458327.102860	0.001263	TESS
3	2458350.929974	0.000904	TESS
4	2458362.843557	0.000851	TESS
5	2458374.749429	0.001078	TESS
13	2458469.975553	0.001690	TESS
14	2458481.884441	0.001284	TESS
20	2458553.368053	0.000957	TESS
21	2458565.287934	0.001310	TESS
29	2458660.678263	0.001081	TESS
30	2458672.594730	0.000921	TESS
37	2458755.954035	0.000926	CHAT
38	2458767.856769	0.001243	CHAT
40	2458791.661596	0.000718	CHAT

The extracted mid-transit time estimates and their precise uncertainties yielded very strong periodic TTVs in the TESS and CHAT data, whose amplitude around the mean period was ~1.2 hr, covering one full TTV superperiod. Table 2 lists the precisely extracted individual transit times and their errors. No significant TLS power is detected in the TESS photometry residuals, meaning that only one planetary companion of TOI-2202 is detectable on the TESS FFI light curves. These results suggest the presence of an additional nontransiting companion in the TOI-2202 systems that is close and massive enough to perturb the Jovian-like transiting planet TOI-2202 b.

4.3. Spectral RV and Activity Indices Analysis

For a period search in the precise RVs and activity indices data of TOI-2202, we computed maximum likelihood periodograms, which calculate the log-likelihood ($\ln \mathcal{L}$) power by optimizing for each test frequency. The MLP algorithm allows for multiple data sets, each with an additive offset and jitter parameters (Baluev 2009; Zechmeister et al. 2019), which makes it more suitable for period analysis of multi-instrument data. We adopted the significance thresholds of the $\Delta \ln \mathcal{L}$ improvements, which correspond to false-alarm probabilities (FAPs) of 10%, 1%, and 0.1%.

Figure 4 shows the MLP periodograms of the combined FEROS and HARPS RVs and activity time series, separately. The PFS data consist of only four RVs and these were not included in the MLP analysis. The MLP periodogram of the combined FEROS and HARPS data shows a strong power at 11.91 days, which is the period of the known transiting planet candidate. The RV residuals, after removing the 11.9 days signal, however, do not indicate the presence of additional significant periodicity in the RV data. No significant activity periodicity is evident in the FEROS and HARPS activity indices. The only exception is the HARPS Na I D activity index data, which show marginally significant $\Delta \ln \mathcal{L}$ at lower frequencies that, however, do not have a counterpart in the HARPS RVs. Thus, we concluded that the MLP analysis of the activity data alone does not suggest that TOI-2202 is an active star.

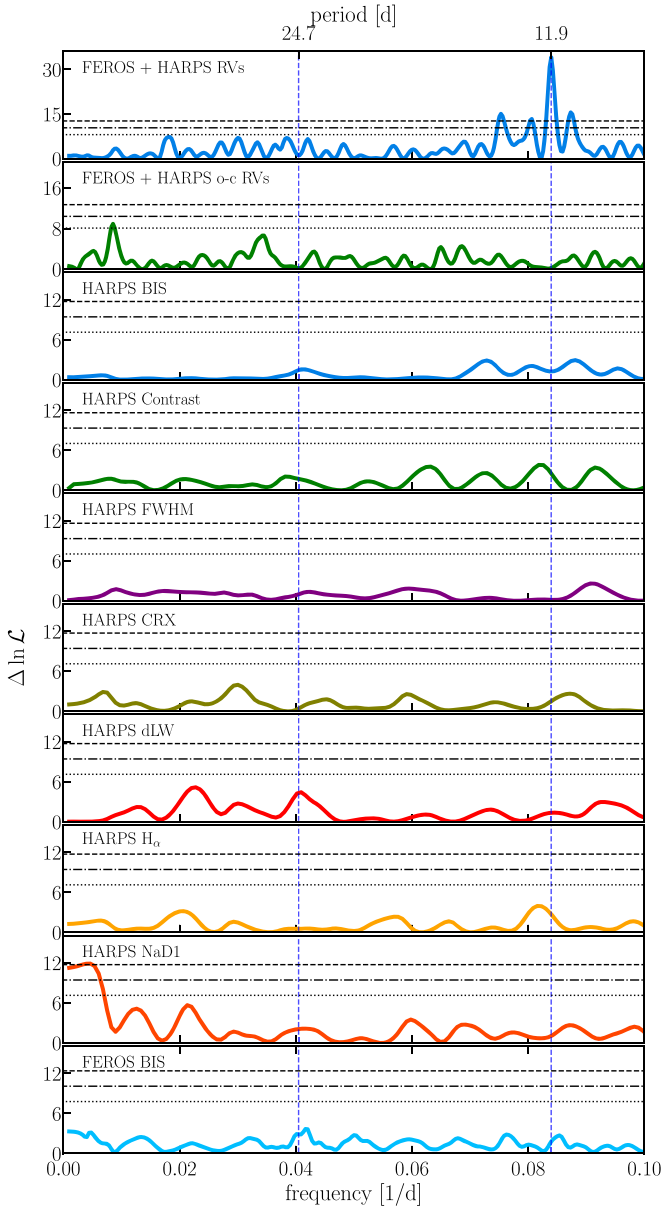

Figure 4. MLP power spectrum for the TOI-2202 data, based on FEROS and HARPS RVs and stellar activity indicators as labeled in the panels. The horizontal lines in the MLP periodograms show the FAP levels of 10%, 1%, and 0.1% in $\Delta \ln \mathcal{L}$. Blue vertical lines indicate the orbital period of TOI-2202 b and c.

Further RV analysis in this work was performed jointly with just the available TTVs (Section 4.4) and transit photometry data (Section 4.5) of TOI-2202, using dynamical modeling.

4.4. Joint TTVs and RV Analysis

Logically, our next step was to study the TTVs obtained from the TESS and CHAT light-curve transit events. TTVs contain essential information of the system's dynamics (Agol et al. 2005), and adequate modeling could reveal the most likely orbital parameters and planetary masses. This is under the condition that at least one complete TTV superperiod (i.e., one cycle of the TTV signal) is covered (Lithwick et al. 2012). We detected just over one full TTV superperiod of the transiting TOI-2202 b, with an estimated period of approximately 357 days. Although this is a promising lead, following Lithwick et al. (2012), it is evident that the observed superperiod and the TTVs amplitude can be explained with almost all possible period ratios in the first- or second-order commensurability, in which TOI-2202 c could be inner or outer planet. Therefore, we examined wide ranges of the period, mass, and eccentricity of the nontransiting TOI-2202 c.

First, we performed TTV fitting with the `Exo-Striker` by adopting a self-consistent dynamical model on the extracted TTVs. The fitted parameters for each planet were the dynamical planetary mass m, orbital period P, eccentricity e, argument of periastron ω, and mean-anomaly M_0, which in this work are always valid for the epoch of the first transit event $t_0 = 2458327.103$ (BJD). For this test we assumed a coplanar, edge-on, and prograde two-planet system (i.e., i_b, $i_c = 90°$ and $\Delta i = 0°$), whereas for the dynamical mass of TOI-2202, we adopted our best estimate of 0.823 $M_\odot$. The time step in the dynamical model was set to 0.1 days to assure a precise orbital resolution of the inner transiting planet TOI-2202 b.

We ran a nested sampling scheme, which allowed us to efficiently explore the complex parameter space of osculating orbital parameters and study the parameter posteriors. In our nested sampling scheme with `dynesty`, we ran 100 "live-points" per fitted parameter, focused on the Bayesian log-evidence convergence, using a "static" nested sampler (see Speagle 2020 for details). For all parameters, we adopted uniform priors, which define an equal probability of occurrence within the experimentally chosen parameter ranges. For TOI-2202 b, we selected prior parameter range estimates taken from our single-planet parameter analysis from Section 4.2, which assure a transit occurrence near $t_0 = 2458327.103$, whereas for the perturber in the system (to become TOI-2202 c), we explored a wide parameter space of eccentricities, masses, and periods. For instance, we explored $P_c \in \mathcal{U}(20.0, 40.0)$ days, $e_c \in \mathcal{U}(0.0, 0.2)$, and $m_c \in \mathcal{U}(0.01, 0.6)$ $M_{\rm Jup}$; the rest of the priors shall not be discussed here for the sake of brevity. However, the prior ranges can be visually assessed in Figure A1, which shows the resultant posterior probability distribution from the TTV analysis. Figure A1 indicates that the posteriors are multi-modal, suggesting that more than one orbital solution could explain the data.

We found that many pairs of planetary masses and eccentricities and orbital periods of TOI-2202 c provide a plausible explanation of the extracted TTVs of TOI-2202 b. The ambiguity in eccentricity versus dynamical planetary mass was already observed in another K-dwarf TESS system consistent with two warm Jovian-mass planets, TOI-216 (Dawson et al. 2019). Based only on the TTVs for this system, Dawson et al. (2019) were unable to firmly decide whether the system is an eccentric pair of a Saturn-mass planet accompanied by a Neptune-mass planet or is composed of a Jovian-mass planet in a 2:1 MMR with a sub-Saturn-mass planet, where both planets are consistent with more circular orbits. Only after securing a large number of RV measurements and expanding the TTV baseline of TOI-216 did Dawson et al. (2021) confirm the latter configuration. From the posterior probability distribution, we found that TTVs of TOI-2202 b are most likely induced by an exterior sub-Saturn, whose orbital period is close to the first-order eccentricity-type 2:1 MMR with the transiting planet. Such a planetary configuration resembles the solution for TOI-216. Nevertheless, as can be seen from Figure A1, at this stage we cannot completely rule out that the TOI-2202 system is more eccentric and

resides in the second-order MMR in the 3:1 period ratio commensurability.

The precise RV measurements that we obtained for TOI-2202 could further constrain the orbital eccentricity and planetary masses, and break the ambiguity. Therefore, as a next step, we included the RV data in the analysis by performing a joint TTV+RV nested sampling analysis, repeating the steps and prior ranges listed above. The RV inclusion in the modeling leads to a more complex model, which now fits the RV semi-amplitude K parameter for each planet, constraining the planetary masses and the RV data offsets and RV jitter parameters for HARPS, PFS, and FEROS, adding six more free parameters. For these, we defined experimentally defined uniform priors of RV off. $\in \mathcal{U}(-140.0, -70.0)$ m s^{-1}, and log-uniform (Jeffreys) priors of RV jitter $\in \mathcal{J}(0.0, 50.0)$ m s^{-1}.

Figure A2 shows the results from this analysis. The posterior probability distribution of the parameters from this test is definitive, suggesting a Jovian–Saturn pair close to the 2:1 MMR. Yet, some fraction of the samples are samples are consistent with configurations at the 3:1 period ratio commensurability. Figure 5 shows the TTV+RV dynamical fit with maximum $-\ln \mathcal{L}$ from the nested sampling posteriors, which is consistent with a pair of massive planets close to the 2:1 MMR. For completeness, we examined the alternative best-fit model near the 3:1 commensurability. Figure 6 shows the competing $\sim$3:1 period ratio best-fit solution. The quality of these fits and overall posterior probability median values and 1σ uncertainties are listed in Table 3. From Figure 5 and Figure 6 it is very clear that a pair close to the 2:1 MMR or the 3:1 MMR can explain the TTV signal. However, the only reasonable solution to the RV data is shown in Figure 5, i.e., the system in the 2:1 commensurability. We note that in both cases shown in Figures 5 and 6 the RV scatter is large, which we attribute to the relatively low S/N of the spectra that we achieved for this rather faint star, but the RV jitter parameter estimates of the HARPS, FEROS, and PFS data are far more reasonable in the 2:1 period ratio case. A visual inspection of Figures 5 and 6 shows that the RV data follows the two-planet dynamical model adequately. The orbital solution close to the 2:1 MMR has $-\ln \mathcal{L} = -136.45$, which is statistically more significant than the one close to the 3:1 MMR, which has $-\ln \mathcal{L} = -159.34$ (i.e., $\Delta \ln \mathcal{L} = 22.9$). Therefore, we conclude that the combination of TTVs from TESS and CHAT, and the RV data from FEROS, HARPS, and PFS, firmly point to a massive pair of Jovian planets with periods of $P_b = 11.9101^{+0.0009}_{-0.0009}$ days, and $P_c = 24.754^{+0.007}_{-0.008}$ days, eccentricities of $e_b = 0.078^{+0.014}_{-0.010}$ and $e_c = 0.011^{+0.009}_{-0.006}$, and dynamical masses of $m_b = 0.927^{+0.035}_{-0.036}$ $M_{\rm Jup}$ and $m_c = 0.191^{+0.032}_{-0.030}$ $M_{\rm Jup}$.

4.5. Joint Photodynamical Analysis of the Transit Light Curves and RV Data

The transit light curves and the RV data of TOI-2202 contain the dynamical signature of the gravitationally interacting planets in the system. Therefore, we performed an alternative, more complex, orbital fitting with respect to the analysis presented in Section 4.4. We adopted a self-consistent photodynamical model that fits directly the transit light curves and RVs in an attempt to extract more accurate estimates of the planetary orbital and physical parameters. This comes at the cost of significantly more CPU time.

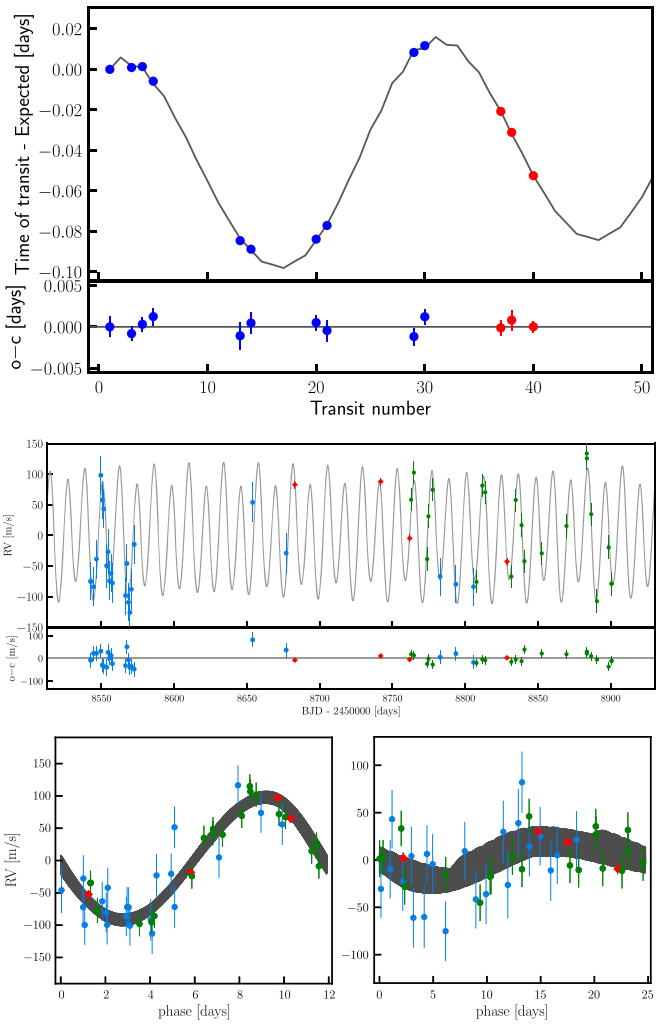

Figure 5. TTVs of TOI-2202 (blue—TESS, red—CHAT) modeled with a two-planet dynamical model jointly with the RVs from FEROS (blue circles), PFS (red diamonds), and HARPS (green circles). The top panel shows the TTV time series and a model consistent with two massive planets with periods close to the 2:1 MMR commensurability. The bottom subpanel shows the TTV residuals. The middle panel shows the same model, but for the Doppler data. The bottom subpanel shows the RV residuals. The bottom left and right panels show a phase-folded representation of the RV data, modeled with the dynamical model (with an osculating period). The data uncertainties include the estimated RV jitter, added in quadrature to the error budget.

We chose to apply the photodynamical model on the raw photometric light curves of TOI-2202, which we simultaneously de-trended during the orbital fitting. We included linear models fit to the CHAT data, which simultaneously de-trend the light curves against airmass at the time of observation, and a GP regression model fit to the TESS transit light curves, which aims to capture the evident stellar activity signals seen in the TESS data (see Section 2.1 and Figure 2). The transit GP model parameters we shared with a GP model applied to the RV time series. The inclusion of a complex transit+RV GP model component to the already complex photodynamical model is well justified, since the TESS light curves exhibit periodicity near the estimated orbital period of TOI-2202 c, which could possibly affect its RV signature and, thereafter, our mass and eccentricity estimates of the planets. This is similar to the case of the GJ 143 system (TOI-186, Dragomir et al. 2019; Trifonov et al. 2019a), for which the TESS light curves and spectroscopy data are consistent with a stellar activity periodicity that is very close to the orbital period of

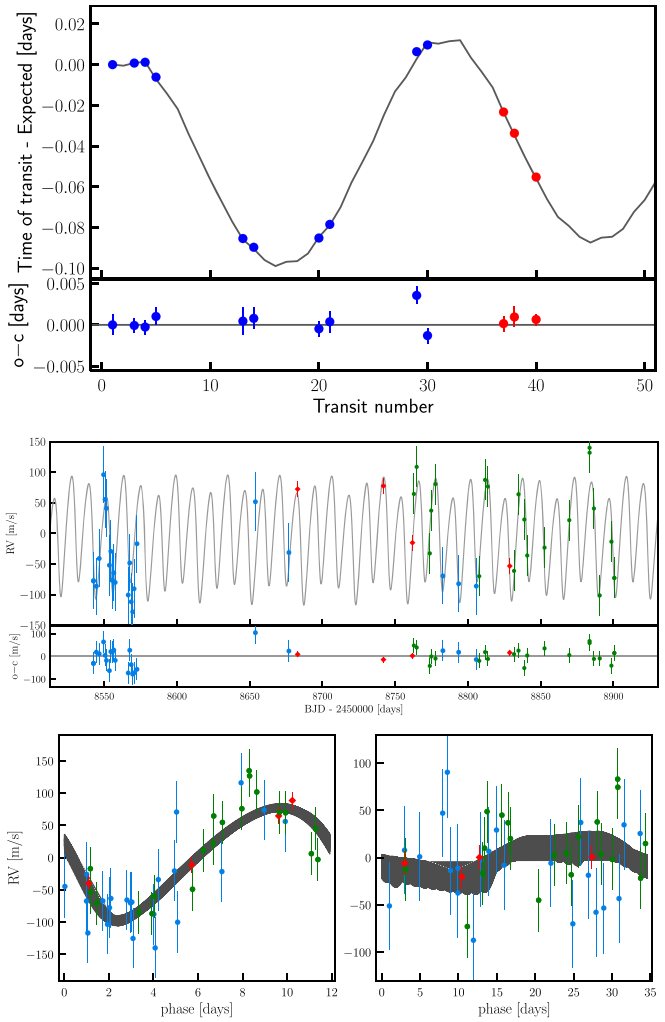

Figure 6. Same as Figure 5, but for an alternative dynamical model consistent with two massive planets with periods close to the 3:1 MMR commensurability (see text for details).

the transiting Neptune-mass planet GJ 143 b (Gan et al. 2021). Although we did not detect significant periodic signals in the spectroscopic activity indices and RVs near the orbital frequency TOI-2202 c, the large RV jitter observed in all three RV data sets motivated us to adopt a "common" GP regression model. For this purpose, we adopted the rotational GP regression kernel as formulated by Foreman-Mackey et al. (2017b):

$$k(\tau) = \frac{B}{2+C} e^{-\tau/L}\left[\cos\left(\frac{2\pi\tau}{P_{\rm rot}}\right) + (1+C)\right], \qquad (1)$$

where $P_{\rm rot}$ is a proxy for the rotation period of the star, L is the coherence timescale (e.g., the life-time of stellar spots), τ is the time lag between two consecutive data points, and C is a balance parameter for the periodic and the nonperiodic parts of the GP kernel. These parameters were set common to the RV and transit light-curve parts of the model. The parameter B defines the GP co-variance amplitude, and thus, naturally, the RV and the transit models have separate amplitude parameters.

Similar to that described in Section 4.4, we performed a nested sampling test, which we used to estimate the fitted parameter posteriors and confidence intervals, with a numerical time step in the dynamical model set to 0.1 days. We fitted the TESS and the CHAT light curves, adopting a central body mass of 0.823 $M_\odot$ and free orbital parameters, which for the two planets are the planetary orbital period P, eccentricity e and argument of periastron ω, and orbital inclination i. The dynamical modeling scheme within the `Exo-Striker` fits the osculating orbital parameters for a given epoch (i.e., nonstatic, perturbed orbital parameters), and thus, it requires the mean-anomaly M_0 parameterization instead of the time of inferior transit conjunction t_0, which is commonly used in Keplerian models when fitting transit light curves. For each sampling iteration, the `Exo-Striker` computes the perturbed orbital elements and transit times, which allows for the precise modeling of the light curves. Since only TOI-2202 b transits, we only fit the light curves with the planetary scaled semimajor axis, $a_b/R_\star$, and radius $R_b/R_\star$, whereas for TOI-2202 c these are unconstrained. However, we allowed i_c to vary in the fitting to account for mutual orbital inclinations, and therefore non-coplanar orbital dynamics. Thus, we allowed TOI-2202 c to transit in our orbital analysis, although such models are naturally penalized by a poorer $-\ln\mathcal{L}$. The fitted orbital parameters for the RV model are shared with those of the transit model, while the RV signal semi-amplitude K parameters for each planet constrain the planetary masses in the dynamical model. For the TESS and the CHAT light curves, we adopted different quadratic limb-darkening models and varied the quadratic limb-darkening parameters u_1 and u_2 for each instrument. We also varied the flux offset and jitter parameter of each transit light curve, and the offset and jitter parameters of each RV data set.

Figure 7 shows the transit component of the photodynamical model constructed together with a GP model for TESS and linear models for CHAT, and constrained by the RV data. Figure 8 shows the RV component of the photodynamical model fitted to the FEROS, the HARPS, and the PFS data, including the GP model component. The final estimates we derived from the joint photodynamical model posterior probability distribution are planetary periods $P_b = 11.9101^{+0.0022}_{-0.0036}$ days and $P_c = 24.674^{+0.026}_{-0.034}$ days, eccentricities $e_b = 0.042^{+0.025}_{-0.008}$ and $e_c = 0.062^{+0.026}_{-0.021}$, and dynamical masses $m_b = 0.978^{+0.063}_{-0.059}$ $M_{\rm Jup}$ and $m_c = 0.369^{+0.103}_{-0.084}$ $M_{\rm Jup}$. The mutual inclination we constrained to $\Delta i = 6.56^{+1.92}_{-2.10}$ deg. We note that the posterior distribution for the mass TOI-2202 c planet is bimodal, with peaks at ∼0.30 $M_{\rm Jup}$ and ∼0.47 $M_{\rm Jup}$. We took the median of this bimodal distribution, meaning that it is possible that the mass uncertainties of TOI-2202 c are slightly underestimated. Also, it shows that a full photodynamical model can also suffer from mass-eccentricity ambiguities. The full set of fitted and derived orbital and physical planetary parameter estimates of TOI-2202 b and c are listed in Table 4. The nuisance parameter estimates from the photodynamical nested sampling analysis are listed in Table A4. [37]

5. Dynamics and Long-term Stability

5.1. Numerical Simulations

We performed a long-term stability and dynamical analysis of the TOI-2202 system using a custom version of the Wisdom–Holman *N*-body algorithm (Wisdom & Holman 1991), which directly adopts and integrates the Jacobi

[37] The `Exo-Striker` session, which contains the photodynamical model, priors, posterior distribution of all 52 fitted parameters, and the final correlation plot are available at https://github.com/3fon3fonov/TOI2202.

Table 3
Exo-Striker Posteriors Probability and Maximum $-\ln\mathcal{L}$ Orbital Parameters Estimates of the Two-planet System TOI-2202

	∼2:1 MMR Fit				∼3:1 MMR Fit			
	Median and 1σ		Max. $-\ln\mathcal{L}$		Median and 1σ		Max. $-\ln\mathcal{L}$	
Parameter	Planet b	Planet c	Planet b	Planet c	Planet b	Planet c	Planet b	Planet c
K (m s^{-1})	$94.2^{+3.4}_{-3.6}$	$15.2^{+2.6}_{-2.4}$	95.3	19.6	$83.1^{+8.0}_{-7.7}$	$22.6^{+2.6}_{-2.7}$	86.9	19.5
P (days)	$11.9108^{+0.0009}_{-0.0009}$	$24.7545^{+0.0073}_{-0.0078}$	11.9103	24.7557	$11.9145^{+0.0009}_{-0.0010}$	$34.6091^{+0.0151}_{-0.0125}$	11.9164	34.5803
e	$0.0782^{+0.0135}_{-0.0097}$	$0.0110^{+0.0094}_{-0.0064}$	0.0672	0.0104	$0.1795^{+0.0184}_{-0.0172}$	$0.1318^{+0.0210}_{-0.0170}$	0.2069	0.1308
ω (deg)	$26.9^{+5.2}_{-5.6}$	$55.7^{+16.9}_{-14.8}$	44.4	103.24	$109.8^{+5.9}_{-4.5}$	$198.9^{+7.1}_{-7.8}$	117.9	205.8
M_0 (deg)	$71.2^{+6.5}_{-5.5}$	$145.8^{+13.3}_{-18.7}$	51.2	101.7	$332.3^{+6.2}_{-8.3}$	$202.8^{+5.6}_{-4.7}$	319.1	200.3
a (au)	$0.0956^{+0.0015}_{-0.0016}$	$0.1558^{+0.0025}_{-0.0026}$	0.0957	0.1558	$0.0957^{+0.0015}_{-0.0016}$	$0.1948^{+0.0031}_{-0.0032}$	0.0957	0.1947
m ($M_{\rm Jup}$)	$0.927^{+0.047}_{-0.048}$	$0.191^{+0.033}_{-0.030}$	0.939	0.246	$0.806^{+0.081}_{-0.081}$	$0.316^{+0.037}_{-0.039}$	0.840	0.271
$\mathrm{RV_{off}}$ FEROS (m s^{-1})	$-126.5^{+7.4}_{-7.1}$		−125.9		$-128.4^{+8.9}_{-7.3}$		−123.5	
$\mathrm{RV_{off}}$ PFS (m s^{-1})	$-76.3^{+3.6}_{-3.7}$		−79.5		$-65.5^{+9.1}_{-11.7}$		−67.0	
$\mathrm{RV_{off}}$ HARPS (m s^{-1})	$-109.7^{+4.7}_{-5.1}$		−110.5		$-111.6^{+6.2}_{-7.2}$		−116.6	
$\mathrm{RV_{jit}}$ FEROS (m s^{-1})	$30.7^{+7.3}_{-5.5}$		29.0		$44.3^{+8.4}_{-6.5}$		45.2	
$\mathrm{RV_{jit}}$ PFS (m s^{-1})	$5.9^{+7.0}_{-5.7}$		5.4		$20.6^{+12.3}_{-6.7}$		12.3	
$\mathrm{RV_{jit}}$ HARPS (m s^{-1})	$19.4^{+4.6}_{-3.8}$		17.4		$31.1^{+7.1}_{-5.1}$		32.0	
$-\ln\mathcal{L}$			−136.448				−159.336	

Note. Two possible orbital configurations could explain the observed data: a system close to the first-order 2:1 MMR and a system close to the second-order 3:1 MMR, with a significant statistical preference to the former. The orbital elements are in the Jacobi frame and are valid for epoch BJD = 2458327.103. Only coplanar and edge-on systems (i_b, $i_c = 90°$ and $\Delta i = 0°$) are assumed. The joint TTV+RV dynamical model accepts a fixed value of the stellar mass (0.823 $M_\odot$); however, the derived planetary posterior parameters of a and m are calculated taking into account the stellar mass uncertainty according to the floor uncertainties predicted by Tayar et al. (2020), listed in Table 1.

orbital elements from the Exo-Striker. Because of the relatively short orbital periods of the TOI-2202 planets, we chose a very small integration time step equal to 0.02 days, which was necessary for the accurate numerical calculation analysis of the dynamical properties of the system. However, this short time step leads to severe numerical overhead, which limited our ability to test the system over the system's estimated age. For example, an N-body integration of the TOI-2202 system for only 10 Myr takes approximately one day on a modern CPU. An educated guess, however, suggests that longer integration times are likely not necessary. The Exo-Striker provides instant Angular Momentum Deficiency (AMD, Laskar & Petit 2017) monitoring, which indicates that given the estimated small orbital eccentricities, semimajor axes, mutual orbital inclination, and planetary masses, the TOI-2202 system is AMD-stable. For more details on the calculation of the AMD-stability criteria, we refer to Laskar & Petit (2017). Additionally, given the estimated semimajor axes and masses in the system, we can calculate the mutual Hill radii of the planets as

$$R_{\rm Hill,m} \approx \sqrt[3]{\frac{(m_b + m_c)}{3M_\star}} \frac{(a_b + a_c)}{2} \approx 0.01 \text{ au} \quad (2)$$

and since a_c–$a_b = 0.06$ au, then the planets have about 6 $R_{\rm Hill,m}$, which is above the ∼3.5 $R_{\rm Hill,m}$ threshold needed for the system to be considered Hill-stable (see, Gladman 1993). In terms of AMD and Hill stability, the TOI-2202 planetary system must be generally stable despite the close planetary orbits. Nevertheless, the AMD and Hill stability criteria do not account for the system's dynamics near mean motion resonances, thus they can only be used as a proxy for long-term stability. Therefore, as a compromise, our long-term stability simulations of the TOI-2202 system were performed for a maximum of 1 Myr by numerically integrating 10,000 randomly chosen samples of the achieved parameter posteriors from the photodynamical modeling scheme. We ran our stability test on a modern 40 CPU Intel Xeon based workstation, which took about four weeks to complete, and which we find to be reasonable for the N-body dynamical analysis in this work.

Given the period ratio of the system close to the 2:1 commensurability, we inspected the first-order MMR angles θ_1 and θ_2 , which are defined as:

$$\theta_1 = \lambda_b - 2\lambda_c + \varpi_b, \;\; \theta_2 = \lambda_b - 2\lambda_c + \varpi_c, \quad (3)$$

where $\varpi_{b,c} = \Omega_{b,c} + \omega_{b,c}$ are the planetary longitudes of periatron and $\lambda_{b,c} = M_{0\rm b,c} + \varpi_{b,c}$ are the mean longitudes. We also monitored for libration of the secular apsidal angle $\Delta\omega$, which is defined as:

$$\Delta\omega = \theta_1 - \theta_2 = \varpi_b - \varpi_c, \quad (4)$$

which indicates if the dynamics of the system is dominated by secular interactions, exhibiting apsidal libration in alignment ($\Delta\omega$ librating around 0°), anti-alignment ($\Delta\omega$ librating around 180°), or an asymmetric libration.

The results from our long-term stability analysis indicate that all examined 10,000 samples are stable for 1 Myr with very similar dynamical behavior. Figure 9 shows the derived posteriors of the dynamical properties of the studied 10,000 samples. The distribution of dynamical parameters reveals low-eccentricity evolution, but despite being close to the 2:1 MMR, the TOI-2202 pair seems to reside outside of the low-order eccentricity-type 2:1 MMR. The mean period ratio evolution is osculating around 2.07, while we did not detect libration of the resonance angles θ_1, θ_2, and the apsidal alignment angle $\Delta\omega$. The posterior distributions of θ_1, θ_2, and $\Delta\omega$ are consistent with circulation, with libration amplitudes between 0° and 360°.

Figure 10 shows a 200 yr extent of the dynamical evolution of the photodynamical fit with a maximum $-\ln\mathcal{L}$ from the

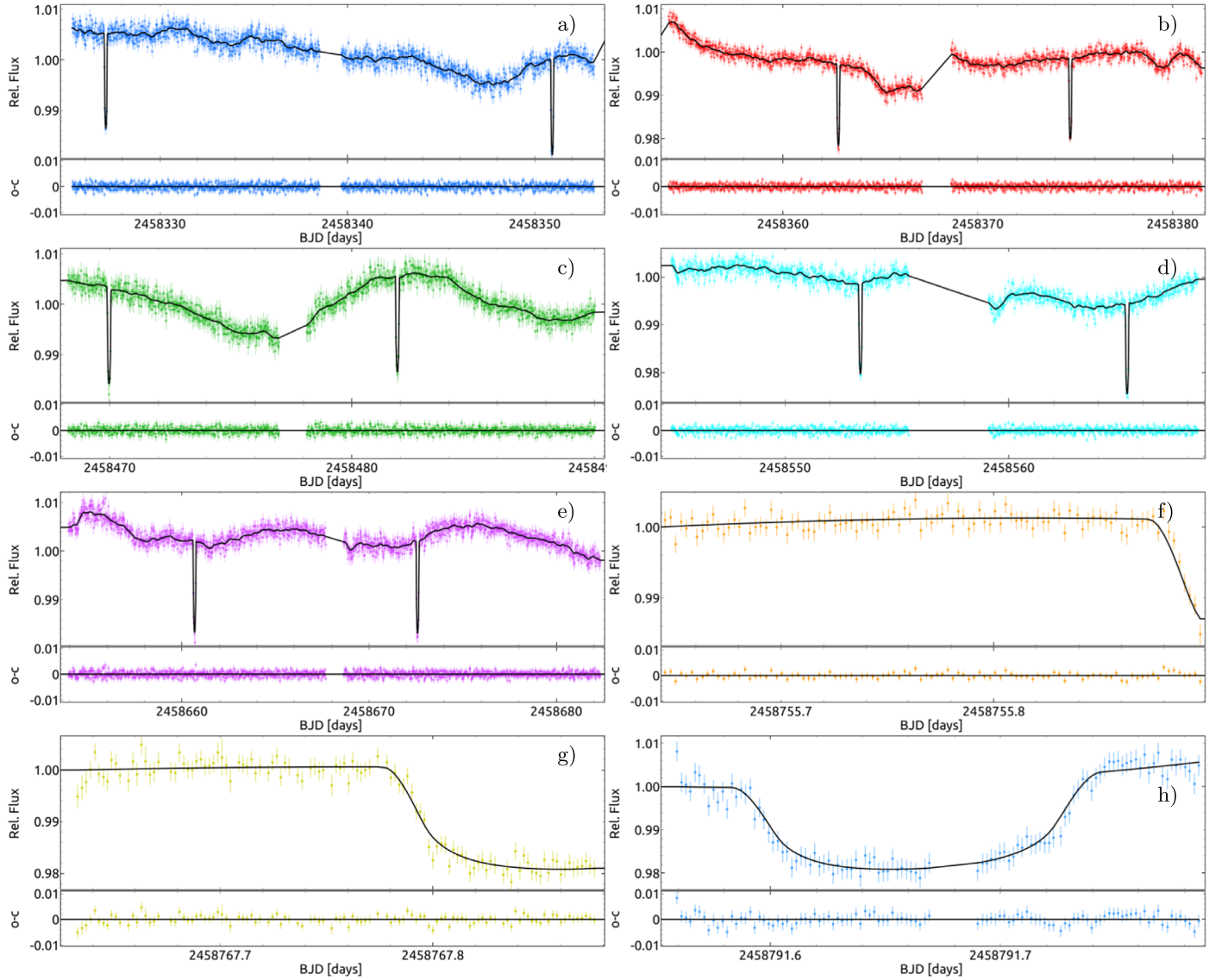

Figure 7. Panels (a)–(e) show TOI-2202's TESS FFI raw photometry data reduced with `tesseract` from Sectors 1 (blue), 2 (red), 6 (green), 9 (orange), and 13 (magenta). Panels (f)–(h) show the three transit events recorded with CHAT. The black curve in the panels shows the global photodynamical model constructed together with the RV model of FEROS, HARPS, and PFS, including a common transit light curve and an RV Gaussian processes regression model that serves as a proxy of the stellar activity (see Figure 8). The CHAT light curves are de-trended against airmass using linear models simultaneously fitted with the rest of the orbital and nuisance data parameters. The subplots of panels (a)–(e) show the residuals between the model (black line) and the respective light-curve data.

posteriors probability samples (see Table 4), which is representative of the overall dynamics of the tested posterior samples. Figure 10 shows the evolution of the semimajor axes a_b and a_c, eccentricities e_b and e_c, the period ratio, the apsidal alignment angle $\Delta\varpi$, and the characteristic 2:1 MMR angles θ_1 and θ_2. No resonance angle libration is observed. For the same fit, Figure 11 shows the trajectory evolution of different combinations of e_b, e_c, and sine and cosine functions of the 2:1 MMR resonance angles θ_1 and θ_2. There is no observed libration around a fixed point in the trajectory evolution that could suggest a 2:1 MMR. Similar trajectory evolution is observed in the majority of the posterior samples that are within the 1σ credible interval.

5.2. Analytical Analysis

The eccentricities of both planets are low and when that is the case, the resonant and near-resonant dynamics can be studied analytically following Nesvorný & Vokrouhlický (2016). There are three variables to consider, each of them being a combination of orbital elements. Constant δ is an orbital invariant that defines the position of the system relative to the 2:1 commensurability, the resonant angle ψ is a combination of θ_1 and θ_2, and variable Ψ is a combination of planetary masses, semimajor axes, and eccentricities (see Nesvorný & Vokrouhlický 2016 for details). Figure 12 shows the position of TOI-2202 in the context of the dynamical variables δ, ψ, and Ψ. The resonant librations of ψ can only happen for $\delta > 0.945$. The best-fit and median values of TOI-2202, listed in Table 4, lead to $\delta \simeq -0.532$ and -0.77, respectively, and the system is therefore firmly outside the libration region. For TOI-2202, Ψ and ψ follow a deformed circle that is slightly offset from the origin, which means that ψ circulates and Ψ oscillates ($0.4 \lesssim \Psi \lesssim 1.1$).

Analytic expressions can be used to relate the TTVs measured for TOI-2202 to the system's architecture. Given

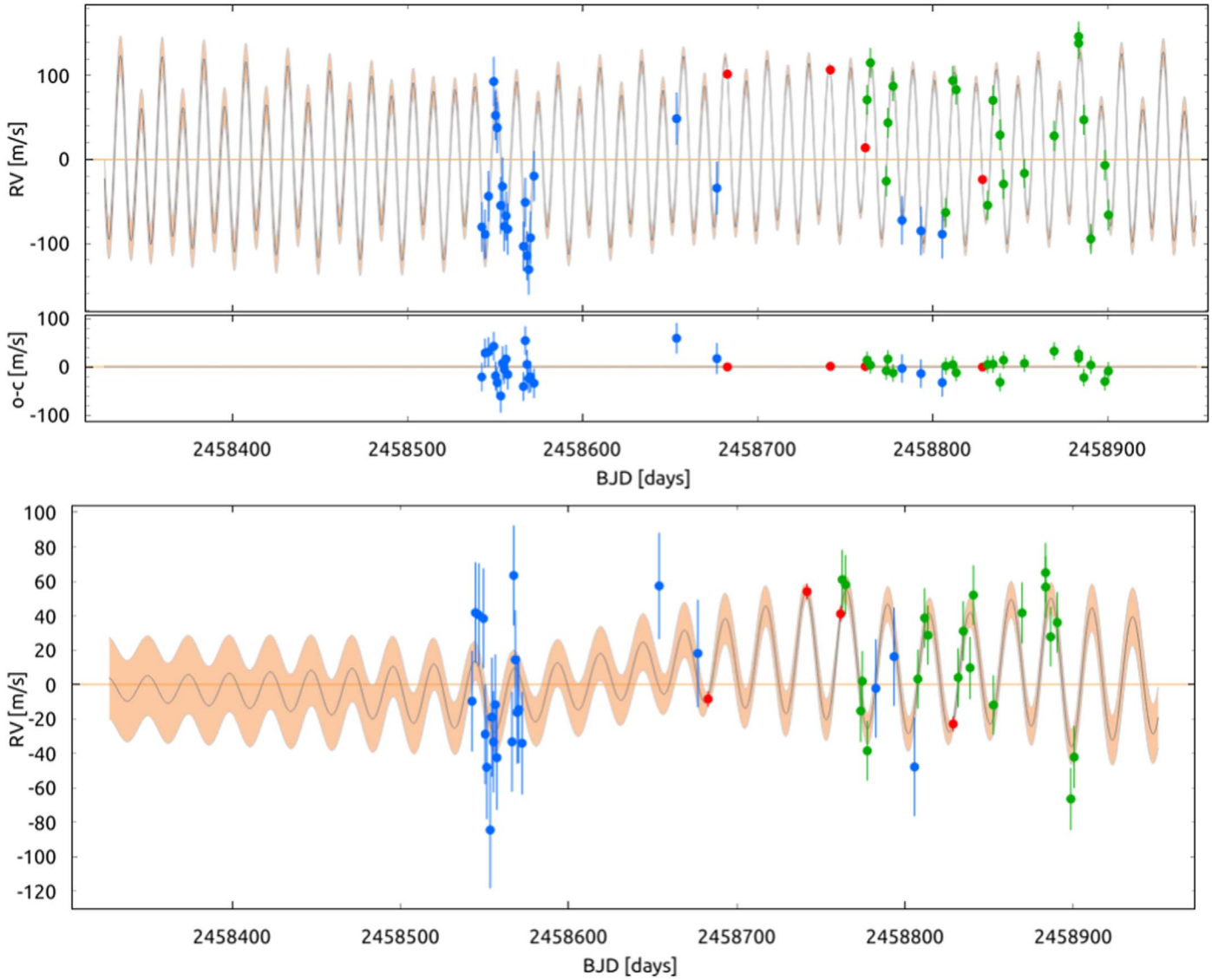

Figure 8. The top panel shows the TOI-2202 RV data from FEROS (blue), HARPS (green), and PFS (red) modeled with a global dynamical model together with the transit light curves of TESS and CHAT including a common RV and transit GP regression model. The subplot to the top panel shows the residuals between the model (black line) and the RV data. The bottom panel shows the GP model component after subtracting the RV counterpart of the dynamical model.

that the two orbits are *not* librating in the 2:1 resonance, here we use analytic TTV expressions given in Agol & Deck (2016). Equation (6) in that paper gives the nonresonant TTVs to the first order in orbital eccentricities. We only consider the highest amplitude term for the inner planet:

$$\delta t_1 = \frac{P_b}{2\pi}\frac{m_c}{M_*} f_{1,1}^{(-2)}\, e_c \sin\theta_2, \tag{5}$$

where $f_{1,1}^{(-2)} \simeq 0.05$. The expected amplitude of TTVs is therefore $A_{\rm TTV} \simeq 0.05$ days, which compares well with the measured amplitude (see Figure 5). Other terms, including TTV chopping during planet conjunctions (Nesvorný & Vokrouhlický 2014; Deck & Agol 2015), are responsible for the slight deviations of measured TTVs from a perfect sinusoid. These terms are important to break degeneracies in the TTV inversion. The expected TTV period is the period of the θ_2 angle. Neglecting the long-term evolution of ϖ_c, the TTV period can be approximated by the superperiod:

$$P_{\rm TTV} = \left[\frac{1}{P_b} - \frac{2}{P_c}\right]^{-1}. \tag{6}$$

Adopting the best-fit orbital periods from Table 4, we obtain $P_{\rm TTV} \simeq 340$ days, which is a good match to Figure 5.

6. Summary and Conclusions

We report the discovery of a compact Jovian-mass pair of planets around the K-dwarf star TOI-2202, for which we estimate a stellar mass of $0.823^{+0.027}_{-0.023}\ M_\odot$ and a radius of $0.794^{+0.007}_{-0.007}\ R_\odot$. This discovery was possible thanks to TESS, which revealed the transiting warm Jovian-mass planet TOI-2202 b that transits with a period of about 11.91 days. The ten TESS transits of TOI-2202 b detected on the FFI, together with three follow-up light curves obtained with the CHAT robotic telescope, show strong TTVs with an amplitude of about 1.2 hr,

Table 4
Nested Sampling Priors, Posteriors, and Maximum $-\ln \mathcal{L}$ Orbital Parameters of the Two-planet System TOI-2202

Parameter	Median and 1σ		Max. $-\ln \mathcal{L}$		Adopted Priors	
	Planet b	Planet c	Planet b	Planet c	Planet b	Planet c
K (m s^{-1})	$99.2^{+5.6}_{-5.2}$	$29.3^{+8.3}_{-6.6}$	92.9	38.3	$\mathcal{U}$(90.0, 110.00)	$\mathcal{U}$(20.0, 40.0)
P (days)	$11.9101^{+0.0022}_{-0.0036}$	$24.6744^{+0.0258}_{-0.0339}$	11.9123	24.6797	$\mathcal{U}$(11.90, 11.92)	$\mathcal{U}$(24.60, 24.80)
e	$0.0420^{+0.0255}_{-0.0075}$	$0.0622^{+0.0452}_{-0.0211}$	0.0672	0.0104	$\mathcal{U}$(0.00, 0.2)	$\mathcal{U}$(0.00, 0.2)
ω (deg)	$84.1^{+9.8}_{-16.4}$	$320.8^{+129.7}_{-12.5}$	86.0	322.6	$\mathcal{U}$(0.0, 360.00)	$\mathcal{U}$(0.0, 360.00)
M_0 (deg)	$7.6^{+26.4}_{-8.5}$	$267.2^{+9.6}_{-269.9}$	4.3	265.8	$\mathcal{U}$(0.0, 360.00)	$\mathcal{U}$(0.0, 360.00)
λ (deg)	$90.4^{+14.6}_{-0.8}$	$226.4^{+7.1}_{-15.5}$	90.3	228.4	(derived)	(derived)
i (deg)	$88.4^{+0.6}_{-3.3}$	$84.7^{+2.4}_{-2.9}$	88.9	87.2	$\mathcal{U}$(80.0, 90.0)	$\mathcal{U}$(80.0, 90.0)
Ω (deg)	0.0	$5.0^{+2.3}_{-2.8}$	0.0	5.9	(fixed)	$\mathcal{U}$(0.0, 10.0)
$a/R_\star$	$23.08^{+2.90}_{-2.18}$	...	23.45	...	$\mathcal{U}$(20.0, 35.00)	...
$R/R_\star$	$0.1261^{+0.068}_{-0.0065}$	...	0.1255	...	$\mathcal{U}$(0.01, 0.25)	...
Δi (deg)	$6.56^{+1.92}_{-2.10}$	...	6.14	...	(derived)	...
a (au)	$0.09564^{+0.00156}_{-0.00161}$	$0.15544^{+0.00255}_{-0.00263}$	0.09569	0.15554	(derived)	(derived)
m ($M_{\rm Jup}$)	$0.978^{+0.0630}_{-0.0588}$	$0.369^{+0.103}_{-0.0836}$	0.917	0.482	(derived)	(derived)
R ($R_{\rm Jup}$)	$1.01^{+0.522}_{-0.080}$	...	0.992	...	(derived)	...

Note. Additionally, these parameters were estimated including a Gaussian processes regression kernel, which was used to model the stellar rotation effects and was common to the TESS light curves and RV data. CHAT light curves were simultaneously modeled with linear regression models to account for airmass optical effects. These and other nuisance parameter estimates are listed in Table A4. The orbital elements are in the Jacobi frame and are valid for epoch BJD = 2458327.103. The joint dynamical model accepts a fixed value for the stellar mass (0.823 $M_\odot$); however, the derived planetary posterior parameters of a, m, and R are calculated taking into account the stellar parameter uncertainties (see the Note in Table 2). The median value of m_c comes from a bimodal distribution (see Figure 9).

suggesting the presence of a second, nontransiting, massive body that perturbs the transiting planet.

A precise Doppler spectroscopy follow-up with FEROS, HARPS, and PFS firmly confirmed the transiting candidate's planetary nature, pointing to a Jovian-mass planet with a dynamical mass of $m_{\rm p} \sim 1.0\ M_{\rm Jup}$. We performed an extensive analysis of the RVs and transit data, and we revealed an outer Saturn-mass companion with a mass $m_{\rm p} \sim 0.4\ M_{\rm Jup}$ and a period of 24.67 days, which puts the warm pair of massive planets near the 2:1 period ratio commensurability. The mass and period of the outer planet, TOI-2202 c, were indirectly revealed thanks to the dynamical orbital analysis, as the available transit and Doppler data did not directly support its presence. From our combined Doppler and photodynamical modeling scheme, we obtained a semi-amplitude $K_c = 29.3^{+8.3}_{-6.6}$ m s^{-1} of TOI-2202 c, which is significant, and given the precision of the RV data, it should have been detected by our MLP period search (see the one-planet RV residuals MLP in Figure 4). We attribute the nondetection of the RV signal induced by TOI-2202 c to the combination of at least four important effects. (1) All RV data sets have a notable white noise in terms of "RV" jitter (see Table A4). The larger variance of the data contributes to reducing the MLP power. (2) The stellar activity seems to strongly influence the TESS light curve and the RV data. We retained a strong quasi-periodic signal with a period of (transit+RV) $\mathrm{GP_{Rot.}} = 24.1^{+2.3}_{-1.8}$ days, and an RV amplitude of $\mathrm{GP_{Rot.}\ Amp.} = 585.3^{+229.1}_{-244.3}$ m^2 s^{-2} ($\sim 24.2^{+15.1}_{-16.6}$ m s^{-1}), which are inconveniently similar to those of TOI-2202 c (see, e.g., the bottom panel of Figure 8). The TOI-2202 case amply demonstrates the modeling difficulties that arise when stellar activity and Doppler planetary signals are nested within similar periods. (3) In Doppler observations, a pair of planets in low-eccentricity orbits near a 2:1 MMR can be misinterpreted as a single planet (Anglada-Escudé et al. 2010; Wittenmyer et al. 2013; Kürster et al. 2015; Boisvert et al. 2018; Hara et al. 2019). Thus, it is possible that some of the signal from TOI-2202 c may have been fit by a change in the estimated eccentricity of TOI-2202 b. (4) Last, but not least, the planets' strong mutual perturbations also impact the MLP period search. The temporal baseline of our RV data is only $\sim$1 yr, within which, however, our N-body simulations reveal strong end-to-end secular variations of, e.g., $2.042 < P_{\rm rat.} < 2.085$, and $110^\circ < \Delta\omega < 150^\circ$, which result in RV signal phase shifts, and period osculation (as well in TTVs). All of these effects contribute to a certain degree in blurring the Doppler-induced planetary signals. While TOI-2202 b is massive enough to induce a notable RV signal, the Doppler signal of the less massive outer planet TOI-2202 c seems to be buried in noise.

Finally, additional nontransiting planets could reside in the system, but we cannot disentangle their complex contribution to the observed RV signal. While such a possibility is valid, we do not have solid evidence that this could be the case. We note that while TOI-2202 b and TOI-2202 c orbit far enough from one another to be stable as a two-planet system, systems with three or more planets require larger separations for stability (e.g., Chambers et al. 1996; Pu & Wu 2015; Petit et al. 2020; Lissauer & Gavino 2021). Thus, if any other planets are present in this system, their orbits are likely to be more distant (in terms of Hill sphere radii) from the two known planets than these two planets are from one another.

Our numerical and analytical dynamical analysis of the system configuration revealed that the Jovian-mass pair is actually outside of the exact 2:1 MMR. We ruled out a 2:1 MMR librating configuration of TOI-2202, based on the available transit and RV data. The osculating period ratio of TOI-2202 is a little above 2, which falls within the peak of the distribution of period ratios of planet pairs observed by Kepler (Lissauer et al. 2011; Fabrycky et al. 2014). However, the Kepler sample is dominated by super-Earths and sub-Neptunes, and not warm, giant planets like TOI-2202 b and c, which have masses consistent with Jupiter and Saturn.

There are several possible scenarios that could explain the nonresonant orbital configuration of the TOI-2202 pair of

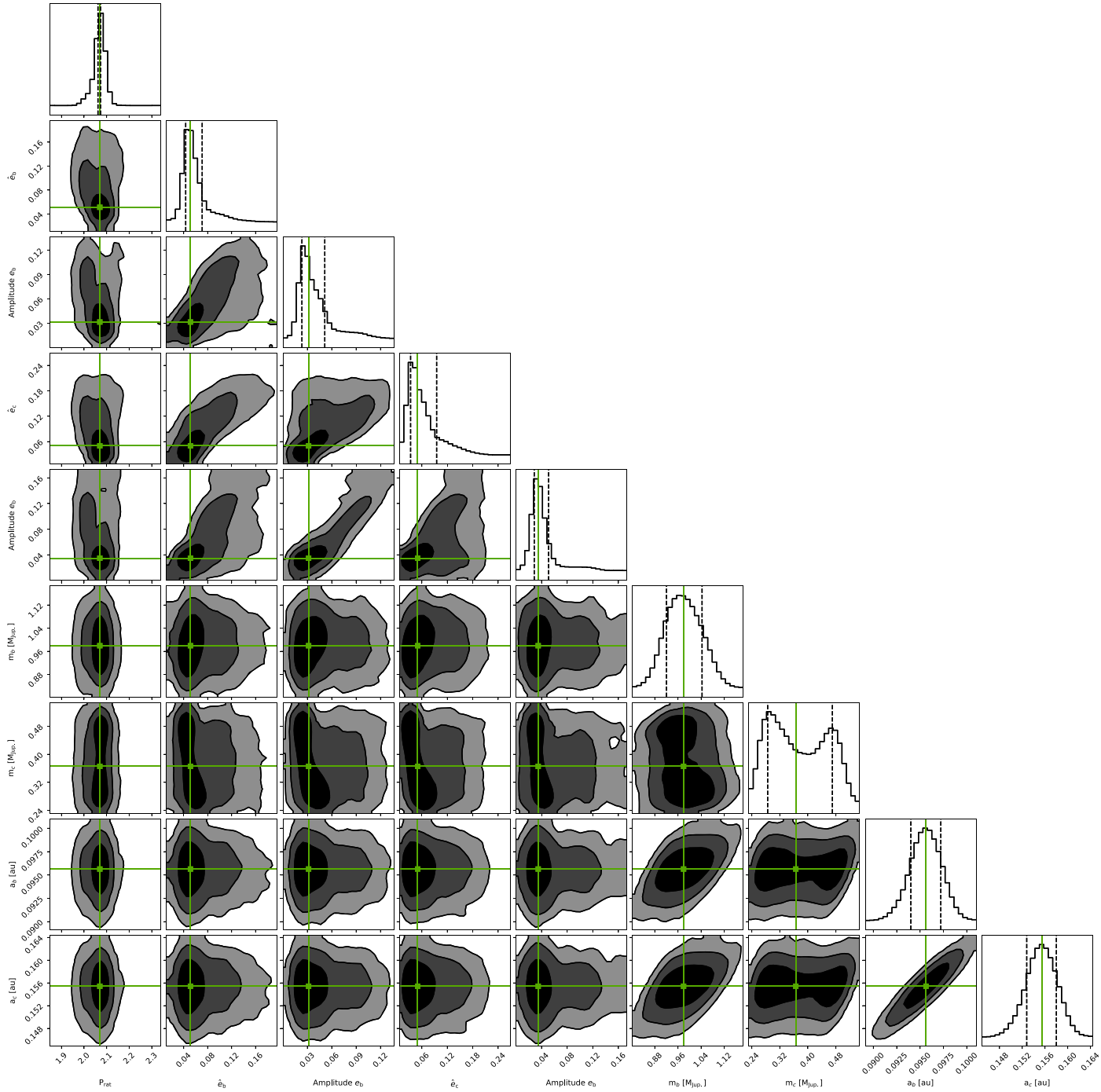

Figure 9. Posteriors of the dynamical properties at the 2:1 period ratio commensurability of the two-planet system TOI-2202 achieved by randomly drawing 10,000 samples from the global posterior of the self-consistent dynamical model. Each sample is tested for stability and the overall dynamical properties at the 2:1 period ratio commensurability evaluated. The derived dynamical parameters are: mean period ratio $P_{\rm rat.}$, mean eccentricities $\hat{e}_{\rm b}$, $\hat{e}_{\rm c}$, their end-to-end amplitudes Ampl. $e_{\rm b}$, Ampl. $e_{\rm c}$, and their dynamical masses and semimajor axes. Note that the mass of TOI-2202 c is bimodal. The posteriors of the 2:1 MMR dynamical parameters $\Delta\omega$, θ_1, and θ_2 are not shown, since these exhibit circulation between 0 and 2π. The black contours on the 2D panels represent the 1σ, 2σ, and 3σ confidence levels of the overall posterior samples, whereas the green crosses indicate the median values of the derived posteriors.

massive planets. (1) The giant planets formed in situ near resonance and did not experience sufficient migration or eccentricity damping to capture them in resonance (Lee et al. 2014; Batygin et al. 2016; Boley et al. 2016). (2) The giant planets migrated but did not get captured into resonance, maybe due to over-stable libration (Goldreich & Schlichting 2014), turbulence in the disk, or perturbations from other planets. (3) The giant planets were once in resonance, but dislodged through a dynamical interaction with one or more undetected other planets in the system (Ford et al. 2005; Raymond et al. 2009; Carrera et al. 2019).

A few known systems similar to TOI-2202 exist. Apart from TOI-216 (Dawson et al. 2019, 2021), another very similar system of a warm Jovian–Saturn-mass pair in a possible 2:1 MMR is HD 27894 (Trifonov et al. 2017), which is a 0.8 $M_{\odot}$ K dwarf with an inner massive pair of planets with periods of

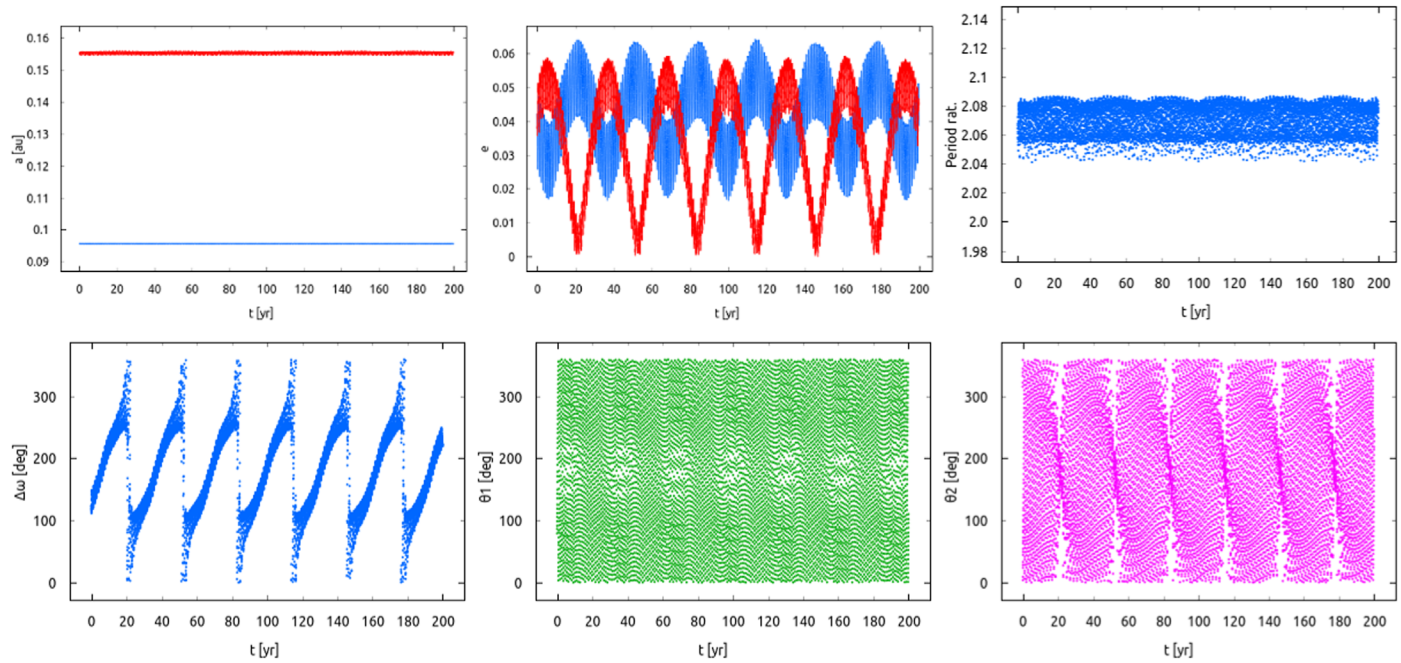

Figure 10. Orbital evolution of the TOI-2202 system for a 200 yr long *N*-body integration using the Wisdom–Holman scheme. Top panels: evolution of the planetary semimajor axes a_b and a_c (left), and the planetary eccentricities e_b and e_c (middle) of the best-fit *N*-body model, and the period ratio (right). Bottom panels: evolution of the apsidal alignment angle $\Delta\varpi = \varpi_b - \varpi_c$ (left), and the resonance angles θ_1 and θ_2 (middle and right). Despite being close to the 2:1 MMR, the pair seems to reside outside of the low-order 2:1 MMR, as no libration in any of the resonance angles is observed and the mean period evolution is osculating above the 2:1 period ratio.

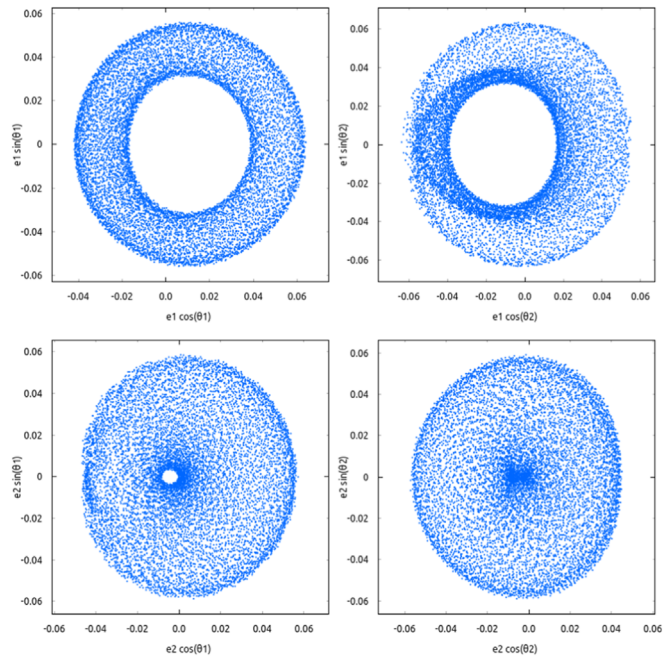

Figure 11. Same as in Figure 10, but represented in the trajectory evolution of different combinations of e_b, e_c, and sine and cosine of the 2:1 MMR resonance angles θ_1 and θ_2. There is no observed libration around a fixed point in the trajectory evolution that could suggest a low-order mean motion resonance in the 2:1 period ratio commensurability.

∼18 days and ∼36 days. The outer planet in the HD 27894 system is ∼4 times less massive than the inner, analogous to TOI-216 and TOI-2202. Then, there is the TOI-2525 system (T. Trifonov et al. 2021, in preparation), which shows a very similar physical configuration to that of TOI-2202. The star TOI-2525 is a K dwarf similar to TOI-2202, and is orbited by a massive pair of an inner Jovian planet and an external Saturn with a period ratio above the 2:1 period ratio commensurability, but which is also not resonant. It seems plausible that such warm, near-resonant systems consistent with a Jovian–Saturn-mass pair are found around K dwarfs.

This research has made use of the Exoplanet Follow-up Observation Program website, which is operated by the California Institute of Technology, under contract with the National Aeronautics and Space Administration under the Exoplanet Exploration Program. Funding for the TESS mission is provided by NASA's Science Mission directorate. This paper includes data collected by the TESS mission, which are publicly available from the Mikulski Archive for Space Telescopes (MAST). Resources supporting this work were provided by the NASA High-End Computing (HEC) Program through the NASA Advanced Supercomputing (NAS) Division at Ames Research Center for the production of the SPOC data products. This work was supported by the DFG Research Unit FOR2544 "Blue Planets around Red Stars," project No. RE 2694/4-1. M.H.L. was supported in part by Hong Kong RGC grant HKU 17305618. A.J., R.B., M.H., and F.R. acknowledge support from ANID—Millennium Science Initiative—ICN12_009. A.J. acknowledges additional support from FONDECYT project 1210718. M.R.D. acknowledges the support by CONICYT-PFCHA/Doctorado Nacional-21140646, Chile. T.D. acknowledges support from MIT's Kavli Institute as a Kavli postdoctoral fellow. J.I.V. acknowledges support of CONICYT-PFCHA/Doctorado Nacional-21191829. D.D. acknowledges support from the TESS Guest Investigator Program grant 80NSSC19K1727 and NASA Exoplanet Research Program grant 18-2XRP18 2-0136. We thank the anonymous reviewer for very helpful comments and suggestions.

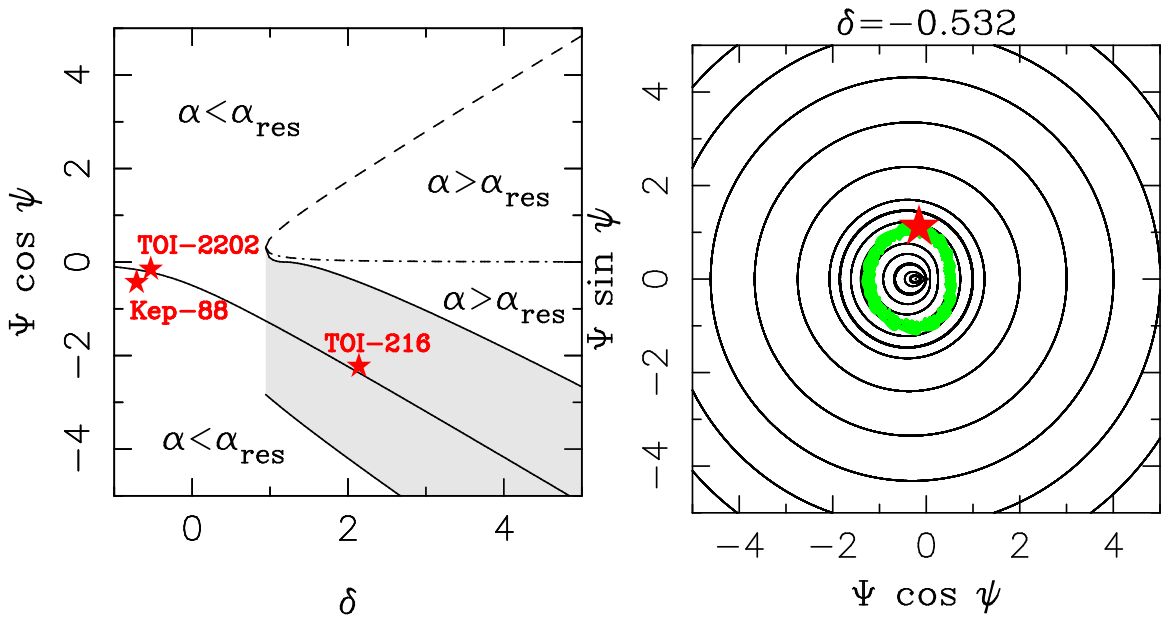

Figure 12. The left panel shows the 2:1 MMR structure diagram following Nesvorný & Vokrouhlický (2016). Three planetary systems are plotted: TOI-2202 (this work), TOI-216 (Dawson et al. 2021), and Kepler-88 (Nesvorný et al. 2013). See Nesvorný & Vokrouhlický (2016) for the definition of parameters δ and Ψ, and the resonant angle ψ. Systems with $\alpha = a_b/a_c < \alpha_{res}$ ($\alpha > \alpha_{res}$), where $\alpha = 0.630$ corresponds to the exact resonance, have orbits just wide (narrow) of the resonance. The resonance region where ψ librates is shaded. The separatrices and stable point are solid. The dotted line is an approximation of the stable point inside the resonance, as explained in Nesvorný & Vokrouhlický (2016). The dashed line is the unstable point, and the dotted–dashed line is the stable point. See Nesvorný & Vokrouhlický (2016) for more explanations. Both TOI-2202 and Kepler-88 are wide of the resonance where ψ circulates. TOI-216 is a resonant system. The right panel shows the trajectory *N*-body orbital evolution of the best photodynamical fit of TOI-2202, mapped onto resonant variables (green dots). The black curves are the analytic approximation of the resonant trajectories from Nesvorný & Vokrouhlický (2016). There is a good correspondence between the numerical and analytical evolutions. The small differences between the two arise due to the neglected terms in the analytic expansion.

Facilities: TESS, CHAT-0.7 m, MPG-2.2 m/FEROS, ESO-3.6 m/HARPS, Magellan-6.5 m/PFS.

Software: Exo-Striker (Trifonov 2019), CERES (Brahm et al. 2017a), ZASPE (Brahm et al. 2017b), tesseract (F. Rojas, in prep.), TESSCut (Brasseur et al. 2019), lightkurve (Lightkurve Collaboration et al. 2018), emcee (Foreman-Mackey et al. 2013), corner.py (Foreman-Mackey 2016), dynesty (Speagle 2020), batman (Kreidberg 2015), celerite (Foreman-Mackey et al. 2017b), wotan (Hippke et al. 2019), transitleastsquares (Hippke & Heller 2019).

Appendix

In this Appendix, we present the additional posterior plots from our global nested sampling fitting to the TTV and Doppler data of TOI-2202, including tables with RVs and activity indices, where applicable. Figure A1 shows the posterior results on the N-body applied to the available TTVs data of TOI-2202. Figure A2 shows the posterior results on the N-body applied to the available TTVs and RV data of TOI-2202. Table A1 shows the FEROS Doppler measurements of TOI-2202, derived from the CERES pipeline. Table A2 shows the HARPS Doppler and activity indices measurements of TOI-2202, as derived by the official ESO-DRS, and the publicly available SERVAL pipelines. Table A3 shows the PFS Doppler measurements of TOI-2202. Table A4 is a continuation of Table 4 listed in the main text. It presents the estimates of the nuisance parameters used in our global modeling.

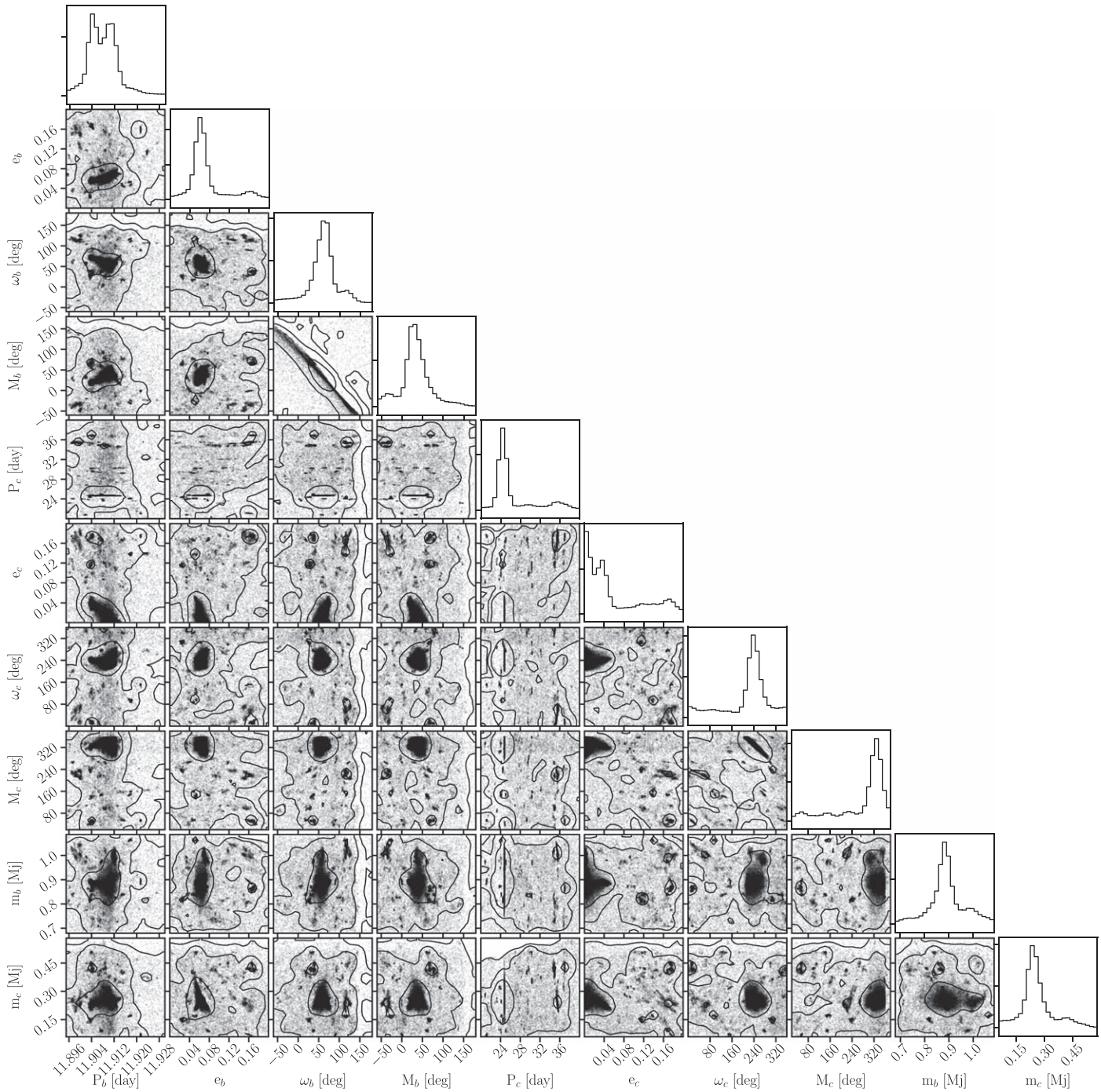

Figure A1. `Exo-Striker` global parameters search results of the TESS and CHAT TTVs of TOI-2202 b done with a nested sampling scheme assuming a coplanar, edge-on, and prograde two-planet system fitted with a self-consistent dynamical model. The black contours on the 2D panels represent the 1σ, 2σ, and 3σ confidence level of the overall nested sampling samples. The distribution of orbital parameters reveals that the observed TTVs of TOI-2202 b are multi-modal, but most likely induced by an exterior Saturn-mass planet whose orbital period is close to the first-order eccentricity-type 2:1 MMR with TOI-2202 b.

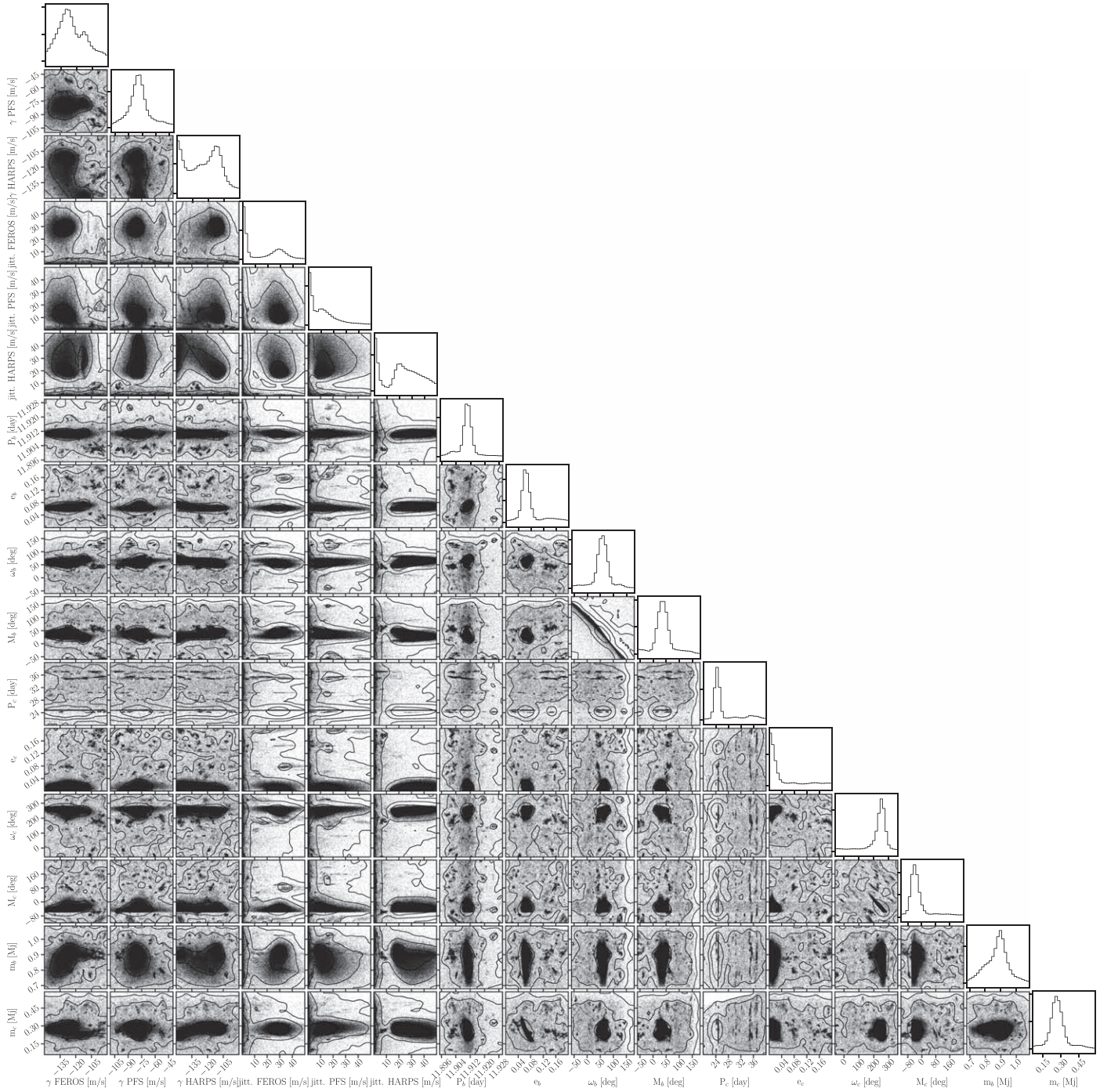

Figure A2. Same as Figure A1 but including the Doppler data in the global nested sampling scheme. The nested sampling distribution shows the distribution of orbital parameters consistent with the FEROS, PFS, and HARPS RV data and the TESS and CHAT TTVs of TOI-2202 b assuming a coplanar, edge-on, and prograde two-planet system fitted with a self-consistent dynamical model. The black contours on the 2D panels represent the 1σ, 2σ, and 3σ confidence level of the overall nested sampling samples.

Table A1
FEROS Doppler Measurements of TOI-2202

Epoch (JD)	RV ($m\,s^{-1}$)	σ_{RV} ($m\,s^{-1}$)
2458542.6107	−201.2	10.7
2458544.5814	−210.0	11.0
2458546.5567	−164.6	12.5
2458549.5470	−27.8	10.5
2458550.5787	−68.1	10.3
2458551.5303	−82.7	13.1
2458553.5551	−175.7	20.2
2458554.5343	−152.9	21.3
2458555.5589	−200.5	11.3
2458556.5614	−188.1	10.6
2458557.5492	−203.7	13.5
2458558.5407	−40.5	18.0
2458559.5642	26.5	14.9
2458566.5039	−224.3	10.0
2458567.5359	−171.9	10.3
2458568.5287	−235.4	10.3
2458569.5235	−251.8	12.1
2458570.5308	−214.1	15.2
2458572.5180	−140.6	12.3
2458653.8986	−72.0	14.6
2458660.8934	−25.6	23.3
2458676.9125	−154.9	15.6
2458782.7537	−193.2	9.2
2458793.5853	−205.9	9.0
2458805.7142	−209.8	8.8

Table A2
HARPS Doppler Measurements of TOI-2202

Epoch (JD)	DRS RV (m s^{-1})	DRS σ_{RV} (m s^{-1})	BIS (m s^{-1})	σ_{BIS} (m s^{-1})	Contrast	$\sigma_{Contrast}$	FWHM (m s^{-1})	σ_{FWHM} (m s^{-1})	SERVAL RV (m s^{-1})	SERVAL σ_{RV} (m s^{-1})	CRX (m s^{-1})	σ_{CRX} (m s^{-1})	dLW (m s^{-1})	σ_{dLW}	H_α	σ_{H_α}	Na I D	$\sigma_{Na\ I\ D}$	Na II D	$\sigma_{Na\ II\ D}$
2458762.8145	−52.26	6.52	10.434	0.104	56.009	0.560	7.255	0.073	54.78	3.31	−12.373	27.905	0.553	1.638	0.525	0.005	0.214	0.006	0.286	0.008
2458764.7474	−8.08	6.55	−35.737	−0.357	55.505	0.555	7.273	0.073	129.14	2.30	6.715	16.390	−0.133	1.152	0.526	0.004	0.263	0.005	0.309	0.006
2458773.7777	−149.33	8.32	−6.315	−0.063	53.973	0.540	7.386	0.074	−81.35	4.07	80.253	46.840	5.546	1.836	0.525	0.006	0.280	0.008	0.335	0.010
2458774.7145	−79.47	7.06	4.569	0.046	55.332	0.553	7.209	0.072	185.53	3.01	−105.263	41.788	9.357	1.488	0.515	0.005	0.233	0.006	0.271	0.007
2458777.6782	−36.10	6.68	−27.291	−0.273	56.648	0.566	7.241	0.072	88.47	4.07	42.774	33.940	0.901	1.807	0.536	0.007	0.293	0.009	0.334	0.010
2458807.7079	−186.62	6.06	−30.652	−0.307	55.845	0.558	7.230	0.072	−44.15	2.61	7.185	20.158	−3.248	1.398	0.521	0.004	0.209	0.005	0.273	0.006
2458811.7423	−29.35	6.56	−2.856	−0.029	56.013	0.560	7.193	0.072	94.87	3.40	9.363	26.927	−1.325	1.567	0.522	0.005	0.202	0.006	0.275	0.008
2458813.7032	−40.23	6.41	10.524	0.105	56.207	0.562	7.229	0.072	69.06	3.40	−3.834	29.515	1.149	1.420	0.530	0.005	0.186	0.006	0.251	0.008
2458831.6523	−177.98	6.45	−20.233	−0.202	55.180	0.552	7.269	0.073	−44.42	2.29	3.715	15.006	−1.157	0.938	0.529	0.004	0.178	0.004	0.256	0.005
2458834.7019	−52.83	6.73	−17.317	−0.173	55.794	0.558	7.272	0.073	75.55	3.15	32.535	24.575	−0.829	1.258	0.530	0.005	0.193	0.006	0.257	0.007
2458838.6934	−94.04	8.57	37.192	0.372	55.380	0.554	7.338	0.073	−15.09	5.24	−37.526	39.004	4.921	2.431	0.532	0.008	0.173	0.010	0.248	0.012
2458840.7025	−152.85	6.55	−21.212	−0.212	55.780	0.558	7.287	0.073	−22.39	2.86	−9.285	23.949	−0.613	1.105	0.533	0.005	0.202	0.005	0.246	0.006
2458852.6085	−139.95	6.32	−7.635	−0.076	55.724	0.557	7.247	0.072	−6.82	2.08	−39.069	15.335	−6.968	1.115	0.530	0.004	0.187	0.004	0.256	0.005
2458869.5997	−95.12	7.62	7.111	0.071	54.063	0.541	7.293	0.073	63.63	2.53	−16.876	26.979	28.673	1.856	0.524	0.004	0.198	0.005	0.272	0.006
2458883.5666	23.19	6.31	−6.497	−0.065	55.299	0.553	7.236	0.072	144.58	3.10	5.812	23.744	−2.980	1.310	0.522	0.005	0.175	0.006	0.266	0.007
2458883.5873	15.10	8.00	−0.441	−0.004	54.625	0.546	7.329	0.073	149.58	3.39	−29.540	26.864	−1.722	1.727	0.534	0.005	0.175	0.006	0.254	0.008
2458886.5552	−76.03	6.81	13.288	0.133	55.998	0.560	7.253	0.073	60.78	3.65	−74.472	27.175	0.324	1.652	0.532	0.006	0.185	0.007	0.266	0.008
2458890.5358	−218.06	7.52	−6.051	−0.061	54.543	0.545	7.352	0.074	−63.98	2.50	−29.871	23.701	−3.326	1.286	0.534	0.004	0.187	0.005	0.253	0.006
2458898.5693	−130.24	8.32	23.765	0.238	55.213	0.552	7.312	0.073	22.72	3.99	−14.593	29.519	−0.539	1.581	0.518	0.006	0.196	0.008	0.254	0.010
2458900.5619	−189.56	8.40	−35.994	−0.360	55.953	0.560	7.259	0.073	−32.42	4.35	47.810	32.842	2.227	2.054	0.537	0.007	0.192	0.009	0.244	0.012

Table A3
PFS Doppler Measurements of TOI-2202

Epoch (JD)	RV (m s^{-1})	σ_{RV} (m s^{-1})
2458682.9274	3.29	2.40
2458741.8941	8.39	2.44
2458761.8289	−84.36	2.43
2458828.7015	−122.43	2.11

Table A4
Continued from Table 4

Parameter	Median and 1σ	Max. $-\ln\mathcal{L}$	Adopted priors
RV $GP_{Rot.}$ Amp. (m^2 s^{-2})	$585.3^{+229.1}_{-244.3}$	615.1	$\mathcal{U}(5.0, 1000.0)$
Transit $GP_{Rot.}$ Amp. (ppm^2)	$576.0^{+1135.0}_{-439.0}$	182.1	$\mathcal{J}(100.0, 2000.0)$
Transit $GP_{Rot.}$ timescale (days)	$150.8^{+23.4}_{-31.2}$	201.0	$\mathcal{J}(100.0, 500.0)$
Transit $GP_{Rot.}$ Period (days)	$24.1^{+2.3}_{-1.8}$	24.3	$\mathcal{U}(20.0, 30.0)$
Transit $GP_{Rot.}$ fact.	$0.0059^{+0.0353}_{-0.0053}$	0.0044	$\mathcal{J}(0.0001, 0.2)$
RV $offset_{FEROS}$ (m s^{-1})	$-119.5^{+10.9}_{-11.3}$	−120.6	$\mathcal{U}(-140.00, -100.00)$
RV $jitter_{FEROS}$ (m s^{-1})	$19.1^{+10.7}_{-15.2}$	26.8	$\mathcal{J}(0.00, 50.00)$
RV $offset_{PFS}$ (m s^{-1})	$-90.1^{+10.7}_{-9.8}$	−98.3	$\mathcal{U}(-110.00, -70.00)$
RV $jitter_{PFS}$ (m s^{-1})	$5.0^{+8.7}_{-3.2}$	3.4	$\mathcal{J}(0.00, 50.00)$
RV $offset_{HARPS}$ (m s^{-1})	$-122.1^{+11.4}_{-9.4}$	−123.3	$\mathcal{U}(-140.00, -100.00)$
RV $jitter_{HARPS}$ (m s^{-1})	$9.8^{+8.2}_{-7.4}$	15.6	$\mathcal{J}(0.00, 50.00)$
Transit $offset_{TESS-S1}$ (ppm)	489^{+1088}_{-1336}	1695	$\mathcal{U}(-2000.0, 2000.0)$
Transit $jitter_{TESS-S1}$ (ppm)	284^{+220}_{-233}	431	$\mathcal{J}(0.0, 1000.0)$
Transit $offset_{TESS-S2}$ (ppm)	-348^{+1372}_{-1229}	−1755	$\mathcal{U}(-2000.0, 2000.0)$
Transit $jitter_{TESS-S2}$ (ppm)	99^{+187}_{-72}	226	$\mathcal{J}(0.0, 1000.0)$
Transit $offset_{TESS-S6}$ (ppm)	-261^{+1230}_{-972}	193	$\mathcal{U}(-2000.0, 2000.0)$
Transit $jitter_{TESS-S6}$ (ppm)	85^{+226}_{-56}	48	$\mathcal{J}(0.0, 1000.0)$
Transit $offset_{TESS-S9}$ (ppm)	-61^{+1185}_{1144}	−1256	$\mathcal{U}(-2000.0, 2000.0)$
Transit $jitter_{TESS-S9}$ (ppm)	100^{+239}_{-70}	161	$\mathcal{J}(0.0, 1000.0)$
Transit $offset_{TESS-S13}$ (ppm)	4619^{+2852}_{-3510}	3039	$\mathcal{U}(-2000.0, 2000.0)$
Transit $jitter_{TESS-S13}$ (ppm)	56^{+140}_{-34}	50	$\mathcal{J}(0.0, 1000.0)$
Transit $offset_{CHAT-1}$ (ppm)	690^{+4946}_{-1714}	260	$\mathcal{U}(-10000.0, 10000.0)$
Transit $jitter_{CHAT-1}$ (ppm)	1688^{+1236}_{-740}	878	$\mathcal{J}(0.0, 5000.0)$
Transit $offset_{CHAT-2}$ (ppm)	-1419^{+3316}_{-1864}	−1436	$\mathcal{U}(-10000.0, 10000.0)$
Transit $jitter_{CHAT-2}$ (ppm)	2289^{+1968}_{-872}	1333	$\mathcal{J}(0.0, 5000.0)$
Transit $offset_{CHAT-3}$ (ppm)	4805^{+2045}_{-2851}	4712	$\mathcal{U}(-10000.0, 10000.0)$
Transit $jitter_{CHAT-3}$ (ppm)	1674^{+1841}_{-1048}	722	$\mathcal{J}(0.0, 5000.0)$
Quad. limb-dark.$_{TESS}$ u_1	$0.49^{+0.19}_{-0.23}$	0.63	$\mathcal{U}(0.00, 1.00)$
Quad. limb-dark.$_{TESS}$ u_2	$0.44^{+0.26}_{-0.25}$	0.05	$\mathcal{U}(0.00, 1.00)$
Quad. limb-dark.$_{CHAT}$ u_1	$0.47^{+0.25}_{-0.23}$	0.22	$\mathcal{U}(0.00, 1.00)$
Quad. limb-dark.$_{CHAT}$ u_2	$0.54^{+0.26}_{-0.28}$	0.89	$\mathcal{U}(0.00, 1.00)$

Note. Nested sampling posteriors and maximum $-\ln\mathcal{L}$ nuisance parameter estimates of the two-planet system TOI-2202 derived by joint dynamical modeling of photometry (TESS, CHAT) and radial velocities (FEROS, PFS, HARPS).

ORCID iDs

Trifon Trifonov https://orcid.org/0000-0002-0236-775X
Rafael Brahm https://orcid.org/0000-0002-9158-7315
Nestor Espinoza https://orcid.org/0000-0001-9513-1449
Thomas Henning https://orcid.org/0000-0002-1493-300X
Andrés Jordán https://orcid.org/0000-0002-5389-3944
David Nesvorny https://orcid.org/0000-0002-4547-4301
Rebekah I. Dawson https://orcid.org/0000-0001-9677-1296
Jack J. Lissauer https://orcid.org/0000-0001-6513-1659
Man Hoi Lee https://orcid.org/0000-0003-1930-5683
Diana Kossakowski https://orcid.org/0000-0002-0436-7833
Felipe I. Rojas https://orcid.org/0000-0003-3047-6272
Melissa J. Hobson https://orcid.org/0000-0002-5945-7975
Paula Sarkis https://orcid.org/0000-0001-8128-3126
Martin Schlecker https://orcid.org/0000-0001-8355-2107
Bertram Bitsch https://orcid.org/0000-0002-8868-7649
Gaspar Á. Bakos https://orcid.org/0000-0001-7204-6727
Mauro Barbieri https://orcid.org/0000-0001-8362-3462
W. Bhatti https://orcid.org/0000-0002-0628-0088
R. Paul Butler https://orcid.org/0000-0003-1305-3761
Jeffrey D. Crane https://orcid.org/0000-0002-5226-787X
Matías R. Díaz https://orcid.org/0000-0002-2100-3257
Stephen Shectman https://orcid.org/0000-0002-8681-6136

Vincent Suc https://orcid.org/0000-0001-7070-3842
Jose I. Vines https://orcid.org/0000-0002-1896-2377
Sharon X. Wang https://orcid.org/0000-0002-6937-9034
George R. Ricker https://orcid.org/0000-0003-2058-6662
Avi Shporer https://orcid.org/0000-0002-1836-3120
Andrew Vanderburg https://orcid.org/0000-0001-7246-5438
Diana Dragomir https://orcid.org/0000-0003-2313-467X
Roland Vanderspek https://orcid.org/0000-0001-6763-6562
Christopher J. Burke https://orcid.org/0000-0002-7754-9486
Tansu Daylan https://orcid.org/0000-0002-6939-9211
Jon M. Jenkins https://orcid.org/0000-0002-4715-9460
Bill Wohler https://orcid.org/0000-0002-5402-9613
Sara Seager https://orcid.org/0000-0002-6892-6948
Joshua N. Winn https://orcid.org/0000-0002-4265-047X

References

Agol, E., & Deck, K. 2016, ApJ, 818, 177
Agol, E., Steffen, J., Sari, R., & Clarkson, W. 2005, MNRAS, 359, 567
Anglada-Escudé, G., López-Morales, M., & Chambers, J. E. 2010, ApJ, 709, 168
Bailer-Jones, C. A. L., Rybizki, J., Fouesneau, M., Mantelet, G., & Andrae, R. 2018, AJ, 156, 58
Baluev, R. V. 2008, MNRAS, 385, 1279
Baluev, R. V. 2009, MNRAS, 393, 969
Baruteau, C., Crida, A., Paardekooper, S. J., et al. 2014, in Protostars and Planets VI, ed. H. Beuther et al. (Tucson, AZ: Univ. of Arizona Press), 667
Batygin, K., Bodenheimer, P. H., & Laughlin, G. P. 2016, ApJ, 829, 114
Bitsch, B., Trifonov, T., & Izidoro, A. 2020, A&A, 643, A66
Boisvert, J. H., Nelson, B. E., & Steffen, J. H. 2018, MNRAS, 480, 2846
Boley, A. C., Granados Contreras, A. P., & Gladman, B. 2016, ApJL, 817, L17
Bonfils, X., Delfosse, X., Udry, S., et al. 2013, A&A, 549, A109
Brahm, R., Espinoza, N., Jordán, A., et al. 2019, AJ, 158, 45
Brahm, R., Jordán, A., & Espinoza, N. 2017a, PASP, 129, 034002
Brahm, R., Jordán, A., Hartman, J., & Bakos, G. 2017b, MNRAS, 467, 971
Brahm, R., Nielsen, L. D., Wittenmyer, R. A., et al. 2020, AJ, 160, 235
Brasseur, C. E., Phillip, C., Fleming, S. W., Mullally, S. E., & White, R. L. 2019, Astrocut: Tools for Creating Cutouts of TESS Images, Astrophysics Source Code Library, ascl:1905.007
Butler, R. P., Marcy, G. W., Williams, E., et al. 1996, PASP, 108, 500
Butler, R. P., Vogt, S. S., Laughlin, G., et al. 2017, AJ, 153, 208
Carrera, D., Raymond, S. N., & Davies, M. B. 2019, A&A, 629, L7
Castelli, F., & Kurucz, R. L. 2004, arXiv:astro-ph/0405087
Chambers, J. E., Wetherill, G. W., & Boss, A. P. 1996, Icar, 119, 261
Coleman, G. A. L., & Nelson, R. P. 2014, MNRAS, 445, 479
Crane, J. D., Shectman, S. A., & Butler, R. P. 2006, Proc. SPIE, 6269, 626931
Crane, J. D., Shectman, S. A., Butler, R. P., et al. 2010, Proc. SPIE, 7735, 773553
Crane, J. D., Shectman, S. A., Butler, R. P., Thompson, I. B., & Burley, G. S. 2008, Proc. SPIE, 7014, 701479
Dawson, R. I., Huang, C. X., Brahm, R., et al. 2021, AJ, 161, 161
Dawson, R. I., Huang, C. X., Lissauer, J. J., et al. 2019, AJ, 158, 65
Deck, K. M., & Agol, E. 2015, ApJ, 802, 116
Deck, K. M., Agol, E., Holman, M. J., & Nesvorný, D. 2014, ApJ, 787, 132
Dong, J., Huang, C. X., Dawson, R. I., et al. 2021, ApJS, 255, 6
Dragomir, D., Teske, J., Günther, M. N., et al. 2019, ApJL, 875, L7
Dumusque, X., Turner, O., Dorn, C., et al. 2019, A&A, 627, A43
ESA 1997, The HIPPARCOS and TYCHO Catalogues, ESA SP-1200 (Noordwijk: ESA)
Espinoza, N., Brahm, R., Henning, T., et al. 2020, MNRAS, 491, 2982
Espinoza, N., Kossakowski, D., & Brahm, R. 2019, MNRAS, 490, 2262
Fabrycky, D., & Tremaine, S. 2007, ApJ, 669, 1298
Fabrycky, D. C., Lissauer, J. J., Ragozzine, D., et al. 2014, ApJ, 790, 146
Fischer, D. A., Howard, A. W., Laughlin, G. P., et al. 2014, in Protostars and Planets VI, ed. H. Beuther et al. (Tucson, AZ: Univ. of Arizona Press), 715
Ford, E. B., Lystad, V., & Rasio, F. A. 2005, Natur, 434, 873
Foreman-Mackey, D. 2016, JOSS, 1, 24
Foreman-Mackey, D., Agol, E., Ambikasaran, S., & Angus, R. 2017a, AJ, 154, 220
Foreman-Mackey, D., Agol, E., Angus, R., & Ambikasaran, S. 2017b, AJ, 154, 220
Foreman-Mackey, D., Hogg, D. W., Lang, D., & Goodman, J. 2013, PASP, 125, 306
Gaia Collaboration, Brown, A. G. A., Vallenari, A., et al. 2018, A&A, 616, A1
Gaia Collaboration, Prusti, T., de Bruijne, J. H. J., et al. 2016, A&A, 595, A1
Gan, T., Wang, S. X., Teske, J. K., et al. 2021, MNRAS, 501, 6042
Gill, S., Wheatley, P. J., Cooke, B. F., et al. 2020, ApJL, 898, L11
Gladman, B. 1993, Icar, 106, 247
Goldreich, P., & Schlichting, H. E. 2014, AJ, 147, 32
Goodman, J., & Weare, J. 2010, Comm. App. Math. Comp. Sci., 5, 65
Guerrero, N. M., Seager, S., Huang, C. X., et al. 2021, ApJS, 254, 39
Hara, N. C., Boué, G., Laskar, J., Delisle, J. B., & Unger, N. 2019, MNRAS, 489, 738
Hippke, M., David, T. J., Mulders, G. D., & Heller, R. 2019, AJ, 158, 143
Hippke, M., & Heller, R. 2019, A&A, 623, A39
Huang, C., Wu, Y., & Triaud, A. H. M. J. 2016, ApJ, 825, 98
Ida, S., & Lin, D. N. C. 2010, ApJ, 719, 810
Jordán, A., Brahm, R., Espinoza, N., et al. 2019, AJ, 157, 100
Jordán, A., Brahm, R., Espinoza, N., et al. 2020, AJ, 159, 145
Kaufer, A., Stahl, O., Tubbesing, S., et al. 1999, Msngr, 95, 8
Kley, W., & Nelson, R. P. 2012, ARA&A, 50, 211
Kossakowski, D., Espinoza, N., Brahm, R., et al. 2019, MNRAS, 490, 1094
Kreidberg, L. 2015, PASP, 127, 1161
Kürster, M., Trifonov, T., Reffert, S., Kostogryz, N. M., & Rodler, F. 2015, A&A, 577, A103
Laskar, J., & Petit, A. C. 2017, A&A, 605, A72
Lee, E. J., Chiang, E., & Ormel, C. W. 2014, ApJ, 797, 95
Lee, M., & Peale, S. 2003, ApJ, 592, 1201
Levison, H. F., Kretke, K. A., & Duncan, M. J. 2015, Natur, 524, 322
Lightkurve Collaboration, Cardoso, J. V. d. M., Hedges, C., et al. 2018, Lightkurve: Kepler and TESS Time Series Analysis in Python, Astrophysics Source Code Library, ascl:1812.013
Lin, D. N. C., & Papaloizou, J. 1986, ApJ, 309, 846
Lissauer, J. J., & Gavino, S. 2021, Icar, 364, 114470
Lissauer, J. J., Ragozzine, D., Fabrycky, D. C., et al. 2011, ApJS, 197, 8
Lithwick, Y., Xie, J., & Wu, Y. 2012, ApJ, 761, 122
Luque, R., Pallé, E., Kossakowski, D., et al. 2019, A&A, 628, A39
Matsumura, S., Brasser, R., & Ida, S. 2021, A&A, 650, A116
Mayor, M., Pepe, F., Queloz, D., et al. 2003, Msngr, 114, 20
Nesvorný, D., Kipping, D., Terrell, D., et al. 2013, ApJ, 777, 3
Nesvorný, D., & Vokrouhlický, D. 2014, ApJ, 790, 58
Nesvorný, D., & Vokrouhlický, D. 2016, ApJ, 823, 72
Pepe, F., Mayor, M., Rupprecht, G., et al. 2002, Msngr, 110, 9
Petit, A. C., Pichierri, G., Davies, M. B., & Johansen, A. 2020, A&A, 641, A176
Petrovich, C., & Tremaine, S. 2016, ApJ, 829, 132
Pu, B., & Wu, Y. 2015, ApJ, 807, 44
Queloz, D., Henry, G. W., Sivan, J. P., et al. 2001, A&A, 379, 279
Rasio, F. A., & Ford, E. B. 1996, Sci, 274, 954
Raymond, S. N., Armitage, P. J., & Gorelick, N. 2009, ApJL, 699, L88
Reffert, S., Bergmann, C., Quirrenbach, A., Trifonov, T., & Künstler, A. 2015, A&A, 574, A116
Ricker, G. R., Winn, J. N., Vanderspek, R., et al. 2015, JATIS, 1, 014003
Santerne, A., Moutou, C., Tsantaki, M., et al. 2016, A&A, 587, A64
Schlecker, M., Kossakowski, D., Brahm, R., et al. 2020a, AJ, 160, 275
Schlecker, M., Mordasini, C., Emsenhuber, A., et al. 2020b, arXiv:2007.05563
Skilling, J. 2004, in AIP Conf. Ser. 735, Bayesian Inference and Maximum Entropy Methods in Science and Engineering, ed. R. Fischer, R. Preuss, & U. V. Toussaint (Melville, NY: AIP), 395
Speagle, J. S. 2020, MNRAS, 493, 3132
Tan, X., Payne, M. J., Lee, M. H., et al. 2013, ApJ, 777, 101
Tayar, J., Claytor, Z. R., Huber, D., & van Saders, J. 2020, arXiv:2012.07957
Teske, J., Díaz, M. R., Luque, R., et al. 2020, AJ, 160, 96
Trifonov, T. 2019, The Exo-Striker: Transit and Radial Velocity Interactive Fitting Tool for Orbital Analysis and N-body Simulations, Astrophysics Source Code Library, ascl:1906.004
Trifonov, T., Kürster, M., Zechmeister, M., et al. 2017, A&A, 602, L8
Trifonov, T., Lee, M. H., Reffert, S., & Quirrenbach, A. 2018, AJ, 155, 174
Trifonov, T., Reffert, S., Tan, X., Lee, M. H., & Quirrenbach, A. 2014, A&A, 568, A64
Trifonov, T., Rybizki, J., & Kürster, M. 2019a, A&A, 622, L7
Trifonov, T., Stock, S., Henning, T., et al. 2019b, AJ, 157, 93
Trifonov, T., Tal-Or, L., Zechmeister, M., et al. 2020, A&A, 636, A74
Udry, S., Dumusque, X., Lovis, C., et al. 2019, A&A, 622, A37
Wang, S., Jones, M., Shporer, A., et al. 2019, AJ, 157, 51
Wisdom, J., & Holman, M. 1991, AJ, 102, 1528
Wittenmyer, R. A., Wang, S., Horner, J., et al. 2013, ApJS, 208, 2
Wittenmyer, R. A., Wang, S., Horner, J., et al. 2020, MNRAS, 492, 377
Zechmeister, M., Dreizler, S., Ribas, I., et al. 2019, A&A, 627, A49
Zechmeister, M., & Kürster, M. 2009, A&A, 496, 577
Zechmeister, M., Reiners, A., Amado, P. J., et al. 2018, A&A, 609, A12